



HAL
open science

Constrained overdamped Langevin dynamics for symmetric multimarginal optimal transportation

Aurélien Alfonsi, Rafaël Coyaud, Virginie Ehrlacher

► **To cite this version:**

Aurélien Alfonsi, Rafaël Coyaud, Virginie Ehrlacher. Constrained overdamped Langevin dynamics for symmetric multimarginal optimal transportation. *Mathematical Models and Methods in Applied Sciences*, In press. hal-03131763

HAL Id: hal-03131763

<https://hal.science/hal-03131763>

Submitted on 4 Feb 2021

HAL is a multi-disciplinary open access archive for the deposit and dissemination of scientific research documents, whether they are published or not. The documents may come from teaching and research institutions in France or abroad, or from public or private research centers.

L'archive ouverte pluridisciplinaire **HAL**, est destinée au dépôt et à la diffusion de documents scientifiques de niveau recherche, publiés ou non, émanant des établissements d'enseignement et de recherche français ou étrangers, des laboratoires publics ou privés.

Constrained overdamped Langevin dynamics for symmetric multimarginal optimal transportation

Aurélien Alfonsi Rafaël Coyaud Virginie Ehrlacher

February 4, 2021

Abstract

The Strictly Correlated Electrons (SCE) limit of the Levy-Lieb functional in Density Functional Theory (DFT) gives rise to a symmetric multi-marginal optimal transport problem with Coulomb cost, where the number of marginal laws is equal to the number of electrons in the system, which can be very large in relevant applications. In this work, we design a numerical method, built upon constrained overdamped Langevin processes to solve Moment Constrained Optimal Transport (MCOT) relaxations (introduced in A. Alfonsi, R. Coyaud, V. Ehrlacher and D. Lombardi, *Math. Comp.* 90, 2021, 689–737) of symmetric multi-marginal optimal transport problems with Coulomb cost. Some minimizers of such relaxations can be written as discrete measures charging a low number of points belonging to a space whose dimension, in the symmetrical case, scales linearly with the number of marginal laws. We leverage the sparsity of those minimizers in the design of the numerical method and prove that any local minimizer to the resulting problem is actually a *global* one. We illustrate the performance of the proposed method by numerical examples which solves MCOT relaxations of 3D systems with up to 100 electrons.

Contents

1	Introduction	2
2	Mathematical properties of MCOT particle problems	3
2.1	MCOT and particle problems	3
2.2	Properties of the set of minimizers of the particle problem	7
3	Overdamped Langevin processes for MCOT particle problems	8
3.1	Properties of general constrained overdamped Langevin processes	8
3.2	Application to MCOT problems	10
4	Numerical optimization method	12
4.1	Time-discretization of constrained overdamped Langevin dynamics	13
4.2	Time step and noise level adaptation procedure	14
4.3	Projection method	15
4.4	Initialization procedure	15
5	Numerical tests	17
5.1	One-dimensional test cases ($d = 1$)	17
5.2	Three-dimensional test cases ($d = 3$)	26
6	Proof of Theorem 1	38
6.1	Tchakaloff’s theorem	38
6.2	Proof of Theorem 1	38

1 Introduction

Optimal transport (OT) problems [44, 47] appear in numerous application fields such as data science [38], finance [3], economics [9, 19, 20] or physics [46]. Hence an increasing interest in developing efficient numerical methods for this types of problems among the applied mathematics community.

In this article, we specifically focus on multi-marginal symmetric optimal transportation problems arising from quantum chemistry. Density Functional Theory (DFT) [37] is one of the most popular theories in quantum chemistry in order to compute the ground state of electrons within a molecule. It is exact in principle, due to the Hohenberg-Kohn theorem, up to the knowledge of the Levy-Lieb functional, which is unfortunately not computable in practice. Hence, a wide zoology of electronic structure models have been developed in the chemistry community where approximations of this Levy-Lieb functional are computed [33]. Actually, it has been recently proved [6, 7, 8, 13, 14, 17, 31] that the semi-classical limit of this Levy-Lieb functional is the solution of a symmetric multi-marginal optimal transport problem which we state now.

For all $p \in \mathbb{N}^*$ (where \mathbb{N}^* denotes the set of positive integers $\{1, 2, 3, \dots\}$), we denote by $\mathcal{P}(\mathbb{R}^p)$ the set of probability measures on \mathbb{R}^p . For $d \in \mathbb{N}^*$, for all $\mu \in \mathcal{P}(\mathbb{R}^d)$ and $M \in \mathbb{N}^*$ a fixed number of marginal laws (the number of electrons in DFT), we will denote the set of M -couplings for μ by

$$\Pi(\mu; M) := \left\{ \pi \in \mathcal{P}((\mathbb{R}^d)^M) : \forall 1 \leq m \leq M, \int_{(\mathbb{R}^d)^{M-1}} d\pi(x_1, \dots, x_M) = d\mu(x_m) \right\}. \quad (1)$$

Let $c : (\mathbb{R}^d)^M \rightarrow \mathbb{R}_+ \cup \{+\infty\}$ be a M -symmetric (i.e. such that for all $(x_1, \dots, x_M) \in (\mathbb{R}^d)^M$, $c(x_1, \dots, x_M) = c(x_{\sigma(1)}, \dots, x_{\sigma(M)})$ for $\sigma \in \mathcal{S}_M$ a M -permutation) non-negative lower semi-continuous (l.s.c.) function. The function c is called hereafter the *cost function*. Then, the multimarginal symmetric optimal transport problem associated to μ , M and c is defined as

$$I(\mu) = \inf_{\pi \in \Pi(\mu; M)} \int_{(\mathbb{R}^d)^M} c(x_1, \dots, x_M) d\pi(x_1, \dots, x_M). \quad (2)$$

In DFT applications, the cost c is defined as the Coulomb cost $c(x_1, \dots, x_M) = \sum_{m_1 < m_2} \frac{1}{|x_{m_1} - x_{m_2}|}$. Then, this multimarginal symmetric optimal transport problem allows to compute the interaction energy between electrons, given an electronic density (equal to $M\mu$), in the Strictly Correlated Electrons (SCE) limit – bringing interest in numerical methods for large multimarginal systems.

A straightforward discretization of problem (2) (using a discretization of the state space \mathbb{R}^d with a discrete d dimensional grid for instance) leads to a linear programming problem, whose size scales exponentially with M . Hence, for large values of M , specific numerical methods have to be used in order to circumvent the curse of dimensionality. Hence, new application or efficiency oriented approaches have been developed for such problems, using entropic relaxation and the Sinkhorn algorithm [4, 5], dual formulations of the problem [34] or sparsity structure of the minimizers of the discrete problems [18, 48], which can be combined with a semidefinite relaxation [22, 23].

In a recent paper [1], the authors considered a relaxation of the optimal transport problem (Moment Constrained Optimal Transport – MCOT) which boils down to considering a particular instance of Generalized Moment Problem [21, 24, 25]. The idea of the proposed approach is to change the discretization approach in the sense the state space \mathbb{R}^d is not discretized anymore, but the marginal constraints in (2) are relaxed into a finite number of moment constraints. Taking advantage of the M -symmetry of the problem, it was proved in [1, Proposition 3.3] that some minimizers of the obtained relaxed problems could be written as discrete measures charging a low number of points which scales independently of M .

Thus, a natural idea inspired from this result is to restrict the minimization set considered in the MCOT problem to the set of probability measures of $(\mathbb{R}^d)^M$ which can be written as discrete

measures charging a low number of points and satisfying the associated moment constraints. The resulting problem, called hereafter the *particle problem*, amounts to optimize the positions of the points and the weights charging the associated Dirac measuresⁱ. In principle, the low number of points needed to obtain a representation of a minimizer to the MCOT problem should help in tackling the curse of dimensionality. However, the non-convexity of the particle problem remains a numerical challenge.

One of the first contribution of this paper is to prove that, despite the non-convexity of the obtained particle problem, any of its local minimizers are actually **global minimizers**. Besides, we prove that the set of local minimizers, which is hence identical to the set of global minimizers, is polygonally connected. This first result is stated in Section 2 of the article.

The second contribution of the paper is to propose a numerical scheme in order to find an optimum solution to the particle problem. The numerical method builds on the use of a constrained overdamped Langevin process projected on a submanifold defined by the constraints of the problem, in the spirit of [11, 27, 28, 29, 30, 49]. Such processes are actually already used in the context of molecular dynamics (for which the constraint is defined through the use of a so-called *reaction coordinate* function). We give in this paper some elements of theoretical analysis justifying the interest of such processes for the resolution of multi-marginal optimal transportation problems and outline the link between such constrained overdamped Langevin processes and entropic regularization of optimal transport problems. This is the object of Section 3. Finally, we present the numerical scheme we consider in this article in Section 4 and the numerical results obtained with this approach in Section 5. Proofs of our main theoretical results are postponed until Section 6.

We want here to stress on the fact that this numerical scheme enabled us to obtain approximations of solutions to (2) for very high-dimensional problems, for instance in cases where $d = 3$ and $M = 100$. Such a method thus appears to be a very promising approach in order to solve large-scale problems in DFT for systems involving a large number of electrons.

Let us point out here that algorithms based on constrained overdamped Langevin dynamics can also be used in principle for the resolution of general multimarginal optimal transport problems and multimarginal martingale optimal transport problems, as there exist an MCOT approximation for both types of problems [1]. In these cases, the number of marginal constraints to be imposed scales linearly in M^{ii} , hence the practical implementation of the numerical method proposed in this paper is more intricate than in the symmetric case studied here, where the number of constraints is independant of M .

2 Mathematical properties of MCOT particle problems

We recall in this section the MCOT problem which was introduced in [1], together with the associated particle problem. We also state here our first theoretical results which describe the set of minimizers associated to the particle problem.

2.1 MCOT and particle problems

As introduced in [1], the Moment Constrained Optimal Transport (MCOT) problem is a particular case of Generalized Moment Problem [25] which may be seen as a relaxation of optimal transport where the marginal constraints are alleviated and replaced by a finite number of moment constraints.

ⁱNote that we use, in this article, the term *particle* to designate a *Dirac measure* (seen in the minimization problem as a vector in $\mathbb{R}_+ \times (\mathbb{R}^d)^M$ accounting for a nonnegative weight and the coordinates of a point in $(\mathbb{R}^d)^M$), and not with the physics meaning that encompasses electrons – the electronic density of which, in the DFT application, would correspond in this article to M times the marginal law μ .

ⁱⁱIn the case of multimarginal martingale optimal transport, if there is no assumption of Markovian relationship between the marginal laws, the scaling in the number of constraints for the approximation of the martingale constraints may be exponential in M .

In the following, we restrain our analysis to symmetrical multimarginal optimal transport for the sake of clarity but let us mention here that the results presented here can be extended to general multimarginal optimal transport, as well as martingale optimal transport.

Let $d \in \mathbb{N}^*$, $\mu \in \mathcal{P}(\mathbb{R}^d)$, $M \in \mathbb{N}^*$ and $c : (\mathbb{R}^d)^M \rightarrow \mathbb{R}_+ \cup \{+\infty\}$ be a lower semi-continuous symmetric function. The MCOT problem is a relaxation of the optimal transport problem (2) which we present now. Let $N \in \mathbb{N}^*$ and let us consider a set $(\phi_n)_{1 \leq n \leq N} \subset L^1(\mathbb{R}^d, \mu; \mathbb{R})$ of N continuous real-valued functions, integrable with respect to μ and called hereafter *test functions*. For all $1 \leq n \leq N$, let us denote by

$$\mu_n = \int_{\mathbb{R}^d} \phi_n(x) d\mu(x), \quad (3)$$

the moments of μ , by

$$\begin{aligned} \Pi(\mu; (\phi_n)_{1 \leq n \leq N}; M) &:= \left\{ \pi \in \mathcal{P}((\mathbb{R}^d)^M) : \right. \\ &\forall 1 \leq n \leq N, \int_{(\mathbb{R}^d)^M} \sum_{m=1}^M |\phi_n(x_m)| d\pi(x_1, \dots, x_M) < \infty, \\ &\left. \int_{(\mathbb{R}^d)^M} \left(\frac{1}{M} \sum_{m=1}^M \phi_n(x_m) \right) d\pi(x_1, \dots, x_M) = \mu_n \right\}, \end{aligned} \quad (4)$$

the set of probability measures on $(\mathbb{R}^d)^M$ for which the mean of the moments against the test functions of the marginal laws are equal to the one of μ , and by

$$\begin{aligned} \Pi^S(\mu; (\phi_n)_{1 \leq n \leq N}; M) &:= \left\{ \pi \in \mathcal{P}((\mathbb{R}^d)^M) : \right. \\ &\forall 1 \leq n \leq N, \int_{(\mathbb{R}^d)^M} \sum_{m=1}^M |\phi_n(x_m)| d\pi(x_1, \dots, x_M) < \infty, \\ &\left. \forall 1 \leq m \leq M, \int_{(\mathbb{R}^d)^M} \phi_n(x_m) d\pi(x_1, \dots, x_M) = \mu_n \right\} \end{aligned} \quad (5)$$

the set of probability measures on $(\mathbb{R}^d)^M$ that have, for each marginal law, the same moments as μ against the test functions.

For technical reasons linked to the fact that the optimal problem is defined on the unbounded state space \mathbb{R}^d , we assume in addition that there exists a non-decreasing non-negative continuous function $\theta : \mathbb{R}_+ \rightarrow \mathbb{R}_+$ satisfying $\theta(r) \xrightarrow{r \rightarrow +\infty} +\infty$ and for which there exists $C > 0$ and $0 < s < 1$ such that for all $1 \leq n \leq N$ and all $x \in \mathbb{R}^d$,

$$|\phi_n(x)| \leq C(1 + \theta(|x|))^s. \quad (6)$$

We finally choose a positive real number $A > 0$ satisfying $A \geq A_0 := \int_{\mathbb{R}^d} \theta(|x|) d\mu(x)$.

Then, the *MCOT problem* is defined by

$$I^N := \inf_{\substack{\pi \in \Pi^S(\mu; (\phi_n)_{1 \leq n \leq N}; M) \\ \frac{1}{M} \int_{(\mathbb{R}^d)^M} \sum_{m=1}^M \theta(|x_m|) d\pi(x_1, \dots, x_M) \leq A}} \int_{(\mathbb{R}^d)^M} c(x_1, \dots, x_M) d\pi(x_1, \dots, x_M). \quad (\text{MCOT}^S)$$

Under appropriate assumptions on the family of test functions $(\phi_n)_{1 \leq n \leq N}$, it is proved in [1] that the value of I^N can be made arbitrarily close to I as N , the number of test functions, goes to infinity. Besides, converging subsequences of minimizers to (MCOT^S) necessarily converge to some minimizer of (2). This is the reason why (MCOT^S) can be seen as a particular discretization approach for the numerical approximation of Problem (2).

Remark 1. It is proved in [1] that the value of I^N does not depend on the value of A provided that A satisfies $A \geq A_0$.

Using the symmetry of the cost c and the marginal constraints, it can be easily checked that I^N is also equal to

$$I^N = \inf_{\substack{\pi \in \Pi(\mu; (\phi_n)_{1 \leq n \leq N}; M) \\ \frac{1}{M} \int_{(\mathbb{R}^d)^M} \sum_{m=1}^M \theta(|x_m|) d\pi(x_1, \dots, x_M) \leq A}} \int_{(\mathbb{R}^d)^M} c(x_1, \dots, x_M) d\pi(x_1, \dots, x_M). \quad (\text{MCOT})$$

Then, from [1, Proposition 3.3], there exists at least one minimizer to problem (MCOT), which can be written as

$$\pi^N = \sum_{k=1}^K w_k \delta_{(x_1^k, \dots, x_M^k)}, \quad (7)$$

for some $0 < K \leq N + 2$, with $w_k \geq 0$ and $x_m^k \in \mathbb{R}^d$ for all $1 \leq m \leq M$ and $1 \leq k \leq K$. Besides, the symmetrized measure associated to π^N , which is defined by

$$\pi_S^N := \frac{1}{M!} \sum_{\sigma \in \mathcal{S}_M} \sum_{k=1}^K w_k \delta_{(x_{\sigma(1)}^k, \dots, x_{\sigma(M)}^k)} \quad (8)$$

where \mathcal{S}_M is the set of permutations of $\{1, \dots, M\}$, is a minimizer to (MCOT^S).

The proof of this result makes use of Tchakaloff's theorem [2, Corollary 2], which is recalled in Theorem 4 in Section 6.1. Note that since $\Pi(\mu; (\phi_n)_{1 \leq n \leq N}; M) \subset \Pi(\mu; M)$, when I is finite, it naturally holds that $I^N \leq I < \infty$.

These theoretical results naturally lead us to consider an optimization problem similar to (MCOT) but where the optimization set is reduced to the set of measures of $\Pi(\mu; (\phi_n)_{1 \leq n \leq N}; M)$ which can be written as discrete measures under the form (7) for some $K \in \mathbb{N}^*$. This naturally leads to the following optimization problem, which we call hereafter the *MCOT particle problem* with K particles:

$$I_K^N := \inf_{(W, Y) \in \mathcal{U}_K^N} \sum_{k=1}^K w_k c(X^k), \quad (\text{MCOT}^K)$$

where

$$\mathcal{U}_K^N := \left\{ (W, Y) \in \mathbb{R}_+^K \times \left((\mathbb{R}^d)^M \right)^K, \quad W = (w_k)_{1 \leq k \leq K}, \quad Y = (X^k)_{1 \leq k \leq K}, \right. \\ \left. \sum_{k=1}^K w_k = 1, \quad \sum_{k=1}^K w_k \vartheta(X^k) \leq A, \quad \forall 1 \leq n \leq N, \quad \sum_{k=1}^K w_k \varphi_n(X^k) = \mu_n \right\}, \quad (9)$$

with, for all $X = (x_1, \dots, x_M) \in (\mathbb{R}^d)^M$ and all $1 \leq n \leq N$,

$$\vartheta(X) := \frac{1}{M} \sum_{m=1}^M \theta(|x_m|) \quad \text{and} \quad \varphi_n(X) := \frac{1}{M} \sum_{m=1}^M \phi_n(x_m). \quad (10)$$

In view of [1, Proposition 3.3], we have $I_K^N = I^N$ as soon as $K \geq N + 2$.

A few remarks are in order at this point.

Remark 2. (i) Considering problem $MCOT^K$ as a starting point for a numerical scheme seems very appealing, especially in contexts when M is large. Indeed, in principle, the resolution of $(MCOT^K)$ only requires the optimization of at most $K(M+1)$ scalars, thus would require the resolution of an optimization problem defined on a continuous optimization set involving a number of parameters which only scales **linearly** with respect to the number of marginal laws. Thus, gradient-based algorithms are natural to consider for the numerical resolution of $(MCOT^K)$, at least for differentiable test functions.

(ii) Problem $MCOT^K$ is highly non-convex, whereas the original MCOT problem (MCOT) reads as a (high-dimensional) linear problemⁱⁱⁱ. This definitely makes the numerical resolution of $(MCOT^K)$ a challenging task. This is the reason why we consider in this article **randomized versions of gradient-based** algorithms for the resolution of $(MCOT^K)$. Nevertheless, strikingly, we prove in this article that, despite the lack of convexity, any local minimizers to the MCOT particle problem (MCOT) are actually **global** minimizers, provided that $K \geq 2N + 6$. This is the object of Section 2.2 to state this result and further mathematical properties of the set of minimizers to $(MCOT^K)$.

The main focus of this article is to propose numerical schemes relying on stochastic versions of gradient-based algorithms in order to find minimizers to the MCOT particle problem. Such numerical schemes actually make use of *constrained overdamped Langevin processes*, which are usually encountered in the context of molecular dynamics simulations [28, 29]. In Section 3, we relate such stochastic processes with MCOT problems and entropic regularizations of the latter.

In numerical tests, and especially in the 3D case, the schemes proposed in this article perform better when using a large number of particles K , with weights w_k assumed to be fixed and equal to $\frac{1}{K}$ which are not optimized upon. That is why we introduce here the resulting optimization, called the *MCOT fixed-weight particle problem* with K particles, which reads as follows:

$$J_K^N := \inf_{\substack{Y := (X^k)_{1 \leq k \leq K} \in ((\mathbb{R}^d)^M)^K, \\ \forall 1 \leq n \leq N, \frac{1}{K} \sum_{k=1}^K \varphi_n(X^k) = \mu_n, \\ \frac{1}{K} \sum_{k=1}^K \vartheta(X^k) \leq A}} \sum_{k=1}^K \frac{1}{K} c(X^k). \quad (\text{MCOT}^K \text{ -fixed weight})$$

Remark 3. (i) Let us stress on the fact that the existence of a solution to $(MCOT^K \text{ -fixed weight})$ is not guaranteed in general. This stems from the fact that there may not exist a set of points $Y = (X^k)_{1 \leq k \leq K}$ satisfying the constraints of problem $(MCOT^K \text{ -fixed weight})$. However, for all $N, K \in \mathbb{N}^*$, it always holds that $J_K^N \geq I_K^N$.

Let however consider $(W, Y) \in \mathcal{U}_{N+2}^N$ a minimizer of $(MCOT^K)$ and assume that the cost c and the test functions ϕ_n are bounded. Then, by rounding the weights w_k to a multiple of $1/K$, and then by using ℓ copies of particles with weight ℓ/K , we can construct $\tilde{Y} = (\tilde{X}^k)_{1 \leq k \leq K}$ such that

$$\frac{1}{K} \sum_{k=1}^K \varphi_n(\tilde{X}^k) \approx \mu_n + \mathcal{O}\left(\frac{1}{K}\right).$$

Thus, \tilde{Y} satisfies the moment constraints of problem $(MCOT^K \text{ -fixed weight})$ up to an error of order $\mathcal{O}\left(\frac{1}{K}\right)$ and achieves a cost that is also $\mathcal{O}\left(\frac{1}{K}\right)$ away from the optimal cost achieved by (W, Y) .

Furthermore, in the limit $K \rightarrow \infty$ optima of problems $(MCOT^K \text{ -fixed weight})$ (with an accepted error $\mathcal{O}\left(\frac{1}{K}\right)$ on the constraints) converge to the optimum of the problem (MCOT).

ⁱⁱⁱMore generally, any non-linear minimization problem can be reframed as a linear minimization problem in a much larger space (the measure space), as $\min_{x \in \mathbb{R}^d} c(x) = \min_{\mathbb{P}} \int_{\mathbb{R}^d} c(y) d\mathbb{P}(y)$.

(ii) Yet, in the numerical experiments in the fixed weight case in 3D, the convergence in K appears to be faster than $\mathcal{O}(\frac{1}{K})$ and even low values of K can give sharp approximations of the optimum of (MCOT).

2.2 Properties of the set of minimizers of the particle problem

The aim of this section is to present the first main theoretical result of this paper, which states some mathematical properties on the set of minimizers of the particle problem MCOT^K .

For any $(W, Y) \in \mathbb{R}_+^K \times ((\mathbb{R}^d)^M)^K$, we define by

$$\mathcal{I}(W, Y) := \sum_{k=1}^K w_k c(X^k),$$

where $W := (w_k)_{1 \leq k \leq K}$ and $Y := (X^k)_{1 \leq k \leq K}$. Problem (MCOT^K) can then be equivalently rewritten as

$$I_K^N = \inf_{(W, Y) \in \mathcal{U}_K^N} \mathcal{I}(W, Y). \quad (11)$$

We begin this section by Theorem 1, which states that for any two elements of \mathcal{U}_K^N , there exists a continuous path with values in \mathcal{U}_K^N which connects these two elements, and such that \mathcal{I} monotonically varies along this path.

Theorem 1. *Let us assume that $K \geq 2N + 6$. Let $(W_0, Y_0), (W_1, Y_1) \in \mathcal{U}_K^N$. Then, there exists a continuous application $\psi : [0, 1] \rightarrow \mathcal{U}_K^N$ made of a polygonal chain such that $\psi(0) = (W_0, Y_0)$, $\psi(1) = (W_1, Y_1)$ and such that the application $[0, 1] \ni t \mapsto \mathcal{I}(\psi(t))$ is monotone.*

In order to explain the main ideas of the proof of Theorem 1, let us remark that, using Tchakaloff's theorem (recalled in Section 6.1), for any measure $\pi \in \Pi(\mu; (\phi_n)_{1 \leq n \leq N}; M)$, satisfying,

$$\int_{(\mathbb{R}^d)^M} \vartheta d\pi \leq A, \quad (12)$$

and charging $K \geq 2N + 6$ points, one can find a measure $\tilde{\pi} \in \Pi(\mu; (\phi_n)_{1 \leq n \leq N}; M)$ charging $N + 3$ points, whose support is included in the one of π , and having the same cost and the same moment against ϑ . Then, the segment $((1-t)\pi + t\tilde{\pi})_{t \in [0, 1]}$ is included in $\Pi(\mu; (\phi_n)_{1 \leq n \leq N}; M)$, charges at most $2N + 6$ points and keeps the cost and the moment against ϑ constant. Besides, let $\tilde{\pi}_0, \tilde{\pi}_1 \in \Pi(\mu; (\phi_n)_{1 \leq n \leq N}; M)$ be two measures with support on at most $N + 3$ points, and such that for $i = 0, 1$, $\tilde{\pi}_i$ satisfies (12). Then, the segment $((1-t)\tilde{\pi}_0 + t\tilde{\pi}_1)_{t \in [0, 1]}$ is included in $\Pi(\mu; (\phi_n)_{1 \leq n \leq N}; M)$, satisfies the inequality constraint (12) for all $t \in [0, 1]$, charges at most $2N + 6$ points, and the cost varies linearly along it. By identifying (W_0, Y_0) with π_0 (resp. (W_1, Y_1) with π_1), one can join π_0 to π_1 by segments (with appropriately defined intermediate measures $\tilde{\pi}_0$ and $\tilde{\pi}_1$) satisfying the constraints, and along which the cost varies linearly. The adaptation of these ideas to vectors $(W_0, Y_0), (W_1, Y_1) \in \mathcal{U}_K^N$, which requires to take into account the displacement of the positions between Y_0 and Y_1 as well as the ordering of the coordinates, is the object of Section 6.2.

A direct consequence of Theorem 1 is then Corollary 2 which states that any local minimizer to problem (11) (or equivalently problem MCOT^K) is actually a *global minimizer* as soon as $K \geq 2N + 6$. In addition, the set of minimizers forms an polygonally connected (and thus arc-connected) set.

Corollary 2. *Let us assume that $K \geq 2N + 6$. Then, any local minimizer of the MCOT particle problem (MCOT^K) is actually a global minimizer. Besides, the set of (local or global) minimizers of the MCOT particle problem (MCOT^K) is an polygonally connected subset of $\mathbb{R}_+^K \times ((\mathbb{R}^d)^M)^K$.*

3 Overdamped Langevin processes for MCOT particle problems

The motivation of this section is twofold: first, the numerical method used in this article for the resolution of the particle problems (MCOT^K) and (MCOT^K -fixed weight) can be seen as a time discretization of constrained overdamped Langevin dynamics, which are usually encountered in molecular dynamics simulation; second, we draw here a link, on the formal level, between the long-time and large number of particles limit of these processes and a regularized version of the MCOT problem (MCOT) using the so-called Kullback-Leibler entropy regularization, very similar to the regularization which is at the core of the Sinkhorn algorithm for the resolution of optimal transportation problem [38].

The objective of Section 3.1 is to recall some fundamental properties of general constrained overdamped Langevin processes. Then, in Section 3.2, we consider specific processes which are related to the MCOT problem presented in Section 2.

3.1 Properties of general constrained overdamped Langevin processes

3.1.1 Definition

Let $p \in \mathbb{N}^*$. Let us first introduce *unconstrained* overdamped Langevin processes in the state space \mathbb{R}^p . Let $(\Omega, \mathcal{F}, \mathbb{P})$ be a probability space. An overdamped Langevin stochastic process is a stochastic process $(Y_t)_{t \geq 0}$ solution to the following stochastic differential equation

$$dY_t = -\nabla V(Y_t) dt + \beta dW_t,$$

where $V : \mathbb{R}^p \rightarrow \mathbb{R}$ is a smooth function, called hereafter the *potential function* of the overdamped Langevin process, $\beta > 0$ is a positive coefficient which is proportional to the square root of the temperature of the system in molecular dynamics ($\beta = \sqrt{2\bar{T}}$ with \bar{T} the temperature), and $(W_t)_{t \geq 0}$ is a p -dimensional Brownian motion.

Constrained overdamped Langevin processes are overdamped Langevin processes whose trajectory is enforced to be included into a given submanifold. In the sequel, we assume that the submanifold is characterized as the zero iso-valued set of a given smooth function $\Gamma : \mathbb{R}^p \rightarrow \mathbb{R}^q$ for some $q \in \mathbb{N}^*$, so that the corresponding submanifold is defined by

$$\mathcal{M} = \{Y \in \mathbb{R}^p, \Gamma(Y) = 0\}.$$

We assume in the sequel that the submanifold \mathcal{M} is arc connected. In addition, let us assume that there exists a neighborhood \mathcal{W} of \mathcal{M} such that, for all $Y \in \mathcal{W}$,

$$G(Y) := \nabla \Gamma(Y)^T \nabla \Gamma(Y) \in \mathbb{R}^{q \times q} \quad (13)$$

is an invertible matrix, where $\nabla \Gamma(Y)_{i,j} = \partial_i \Gamma_j$ for $1 \leq i \leq p$ and $1 \leq j \leq q$. These two assumptions on the function Γ , together with the implicit function theorem, imply that \mathcal{M} is a regular $(p - q)$ -dimensional submanifold.

A constrained overdamped Langevin process [28, Section 3.2.3] is a \mathbb{R}^p -valued stochastic process $(Y_t)_{t \geq 0}$ that solves the stochastic differential equation

$$\begin{cases} dY_t = -\nabla V(Y_t) dt + \beta dW_t + \nabla \Gamma(Y_t) d\Lambda_t, \\ \Gamma(Y_t) = 0, \end{cases} \quad (14)$$

where $\beta > 0$, $(W_t)_{t \geq 0}$ is a p -dimensional Brownian process and $(\Lambda_t)_{t \geq 0}$ is a q -dimensional stochastic adapted stochastic process, which ensures that Y_t belongs to the submanifold \mathcal{M} almost surely for all $t \in \mathbb{R}^+$. More precisely, Λ_t is the Lagrange multiplier associated to the constraint $\Gamma(Y_t) = 0$ and is defined by

$$d\Lambda_t = G^{-1}(Y_t) \left[\left(\nabla \Gamma(Y_t)^T \nabla V(Y_t) - \frac{\beta^2}{2} \begin{pmatrix} \sum_{i=1}^p \partial_i^2 \Gamma_1(Y_t) \\ \vdots \\ \sum_{i=1}^p \partial_i^2 \Gamma_q(Y_t) \end{pmatrix} \right) dt - \beta \nabla \Gamma(Y_t)^T dW_t \right]. \quad (15)$$

Thus, if we define $P(y) = \text{Id} - \nabla\Gamma(y)^T G^{-1}(y) \nabla\Gamma(y)$ the projection operator, we get

$$dY_t = P(Y_t)[- \nabla V(Y_t) + \beta dW_t] - \frac{\beta^2}{2} \nabla\Gamma(Y_t)^T G^{-1}(Y_t) \begin{pmatrix} \sum_{i=1}^p \partial_i^2 \Gamma_1(Y_t) \\ \vdots \\ \sum_{i=1}^p \partial_i^2 \Gamma_q(Y_t) \end{pmatrix} dt.$$

Let us assume in addition that

$$Z := \int_{\mathbb{R}^p} e^{-\frac{2V(Y)}{\beta^2}} d\sigma_{\mathcal{M}}(Y) < +\infty, \quad (16)$$

where $d\sigma_{\mathcal{M}}$ is the surface measure (induced by the Lebesgue measure in \mathbb{R}^p , see [28, Remark 3.4] for a precise definition) on the submanifold \mathcal{M} . Let us introduce the probability measure $\eta \in \mathcal{P}(\mathbb{R}^p)$ defined by

$$d\eta(Y) := \frac{1}{Z} e^{-\frac{2V(Y)}{\beta^2}} |\det G(Y)|^{-1/2} d\sigma_{\mathcal{M}}(Y). \quad (17)$$

Under suitable assumptions, [28, Proposition 3.20] states that η is the unique equilibrium distribution of the stochastic process Y_t solution to the constrained overdamped Langevin dynamics (14) and that

$$Y_t \text{ weakly converges to } \eta \text{ as } t \rightarrow +\infty. \quad (18)$$

3.1.2 Long-time and large number of particles limit

We recall here some results proved in [43, Section 2.3 and Proposition 5.1], where the authors consider the so-called large-particle limit of constrained overdamped Langevin dynamics subject to average moment constraints. The objective of the work [43] was to study the properties of the constrained overdamped Langevin process in a large number of particles limit and to show the convergence towards η of the invariant distribution of the approximating particle system when the number of particles $K \rightarrow \infty$.^{iv} More precisely, from now on, let us consider $p' = Kp$ for some $K \in \mathbb{N}^*$. We define for any $K \in \mathbb{N}^*$ the potential function V^K and the constraint function Γ^K by:

$$\forall Y = (X^k)_{1 \leq k \leq K} \in (\mathbb{R}^p)^K, \quad V^K(Y) := \frac{1}{K} \sum_{k=1}^K V(X^k) \quad \text{and} \quad \Gamma^K(Y) := \frac{1}{K} \sum_{k=1}^K \Gamma(X^k).$$

We then consider the following constrained overdamped Langevin process $(Y_t^K)_{t \geq 0}$ that is assumed to be solution to the stochastic differential equation

$$\begin{cases} dY_t^K = -\nabla V^K(Y_t^K) dt + \beta dW_t^K + \nabla \Gamma^K(Y_t^K) d\Lambda_t^K, \\ \Gamma^K(Y_t^K) = 0, \end{cases} \quad (19)$$

where $(W_t^K)_{t \geq 0}$ is a Kp -dimensional Brownian process and $(\Lambda_t^K)_{t \geq 0}$ is a q -dimensional stochastic adapted process, which ensures that Y_t^K satisfies the constraint $\Gamma^K(Y_t^K) = 0$ almost surely. The process Y^K is usually called a particle system: each coordinate X^k for $1 \leq k \leq K$ is seen as a particle. The large number of particles limit consists in considering the limit as K goes to infinity of the stochastic process $(Y_t^K)_{t \geq 0}$.

It follows from (18) that, under suitable assumptions, as t goes to ∞ , the law of the process Y_t^K converges to the probability measure $\eta^K \in \mathcal{P}((\mathbb{R}^p)^K)$ defined for all $Y^K = (X^1, \dots, X^K) \in (\mathbb{R}^p)^K$ by

$$d\eta^K(Y^K) = \frac{1}{Z^K} \left(\prod_{k=1}^K e^{-\frac{2V(X^k)}{\beta^2}} \right) d\sigma_{\mathcal{M}^K}(Y^K), \quad (20)$$

^{iv}We use here the notation K for the number of particles in view of the use of the Langevin dynamics to solve (MCOT^K) problems, from Section 3.2, for which $K \geq 2N + 6$. Yet, the results recalled in Section 3.1.2 are general and unrelated to MCOT applications.

where

$$\begin{aligned}\mathcal{M}^K &:= \{Y^K \in (\mathbb{R}^p)^K, \Gamma^K(Y^K) = 0\}, \\ Z^K &:= \int_{(\mathbb{R}^p)^K} e^{-\frac{2V^K(Y^K)}{\beta^2}} d\sigma_{\mathcal{M}^K}(Y^K),\end{aligned}$$

and

$$G^K(Y^K) := \nabla \Gamma^K(Y^K)^T \nabla \Gamma^K(Y^K) \in \mathbb{R}^{q \times q}.$$

For $1 \leq k \leq K$, $(X_t^k)_{t \geq 0}$ is a p -dimensional stochastic process. Let us denote by $\zeta_t^K \in \mathcal{P}(\mathbb{R}^p)$ the law of the first particle X_t^1 . Then, the symmetry of the functions V^K and Γ^K implies that ζ_t^K weakly converges in law when $t \rightarrow \infty$ to the probability measure ζ_∞^K defined for all $X \in \mathbb{R}^p$ by

$$d\zeta_\infty^K(X) = \int_{(\mathbb{R}^p)^{K-1}} d\eta^K(X, X^2, \dots, X^K). \quad (21)$$

Under appropriate assumptions on V and Γ which we do not detail here [43, Proposition 5.1], the sequence $(\zeta_\infty^K)_{K \in \mathbb{N}^*}$ weakly converges in $\mathcal{P}(\mathbb{R}^p)$ as K goes to infinity to a probability measure $\pi_\beta^* \in \mathcal{P}(\mathbb{R}^p)$ which is the unique solution to

$$\pi_\beta^* := \arg \min_{\substack{\pi \in \mathcal{P}(\mathbb{R}^p) \\ \int_{\mathbb{R}^p} \Gamma d\pi = 0}} \int_{\mathbb{R}^p} \ln \left(\frac{d\pi(X)}{(Z^\infty)^{-1} e^{-\frac{2V(X)}{\beta^2}} dX} \right) d\pi(X), \quad (22)$$

where $Z^\infty := \int_{\mathbb{R}^p} e^{-\frac{2v(X)}{\beta^2}} dX$. In other words, π_β^* is thus a probability measure on \mathbb{R}^p , which is absolutely continuous with respect to the Lebesgue measure and which is solution to

$$\pi_\beta^* := \arg \min_{\substack{\pi \in \mathcal{P}(\mathbb{R}^p) \\ \int_{\mathbb{R}^p} \Gamma d\pi = 0}} \int_{\mathbb{R}^p} V(X) d\pi(X) + \frac{\beta^2}{2} \int_{\mathbb{R}^p} \ln \left(\frac{d\pi(X)}{dX} \right) d\pi(X). \quad (23)$$

3.2 Application to MCOT problems

The aim of this section is to illustrate the link between the MCOT problems presented in Section 2 and the constrained overdamped Langevin processes introduced in Section 3.1. We start by considering the *fixed weight MCOT particle problem* (MCOT^K-fixed weight), before considering the MCOT particle problem with adaptive weights (MCOT).

3.2.1 Fixed-weight MCOT particle problem

We first draw the link between constrained Langevin overdamped dynamics and the fixed weight MCOT particle problem (MCOT^K-fixed weight). Then, for all $K \in \mathbb{N}^*$, let us consider $(Y_t^K)_{t \geq 0}$ a constrained overdamped Langevin process solution to the stochastic differential equation (19) with $p = dM$, $q = N$, $V = c$ and $\Gamma = (\varphi_1 - \mu_1, \dots, \varphi_N - \mu_N)$ where for all $1 \leq n \leq N$, φ_n is defined by (10).

Then, the stochastic dynamics (19) can be viewed as a randomized version of a constrained gradient numerical method for the resolution of problem (MCOT^K-fixed weight), where for all $t \geq 0$, $Y_t^K = (X_t^1, \dots, X_t^K) \in ((\mathbb{R}^d)^M)^K$ and where for all $1 \leq k \leq K$,

$$X_t^k = (x_{1,t}^k, \dots, x_{M,t}^k) \in (\mathbb{R}^d)^M.$$

Note that it is not clear in general that V and Γ satisfy the regularity assumptions which ensure the convergence results stated in Section 3.1.2 to hold true. But, formally, assuming that the long-time limit and large number of particles convergence holds nevertheless, the associated measure π_β^* solution (23) can be equivalently rewritten as

$$\pi_\beta^* := \underset{\substack{\pi \in \mathcal{P}((\mathbb{R}^d)^M) \\ \forall 1 \leq n \leq N, \int_{(\mathbb{R}^d)^M} \varphi_n d\pi = \mu_n}}{\operatorname{arg\,min}} \mathcal{J}(\pi), \quad (24)$$

where

$$\mathcal{J}(\pi) := \int_{(\mathbb{R}^d)^M} c(X) d\pi(X) + \frac{\beta^2}{2} \int_{(\mathbb{R}^d)^M} \ln \left(\frac{d\pi(X)}{dX} \right) d\pi(X).$$

Recall that π_β^* is the large number of particles limit of the long-time limit of the law of one particle associated to the constrained overdamped Langevin process. Notice that π_β^* can be equivalently seen as the solution of an entropic regularization of the MCOT problem (MCOT), where the term $\int_{(\mathbb{R}^d)^M} \ln \left(\frac{d\pi(X)}{dX} \right) d\pi(X)$ can be identified as the Kullback-Leibler entropy of the measure π with respect to the Lebesgue measure. Thus, Problem 24 is close to the entropic regularization of optimal transport problems used in several works [4, 16, 35, 38], in particular for the so-called Sinkhorn algorithm [4].

Let us point out here that, at least on the formal level, we expect the family $(\pi_\beta^*)_{\beta>0}$ to weakly converge to a minimizer of (MCOT) as β goes to 0 (a similar result is proven in [10, Theorem 2.7]).

3.2.2 Adaptive-weight MCOT particle problem

A similar link can be drawn between constrained Langevin overdamped dynamics and the MCOT particle problem (MCOT^K) with adaptive weights.

In order to fit in the framework of the constrained Langevin overdamped dynamics, without any positivity constraint, let us introduce a continuous surjective function $f : \mathbb{R} \rightarrow \mathbb{R}_+$, which we call hereafter a *weight function*. We assume that f satisfies the following assumption: there exists an interval $I \subset \mathbb{R}$ such that the Lebesgue measure of I is equal to 1 and such that $\int_I f = 1$. A simple choice of admissible weight function can be given by $f(a) = a^2$ for all $a \in \mathbb{R}$ with $I = (\frac{1}{2}, \frac{25^{1/3}}{2})$.

Then, for all $K \in \mathbb{N}^*$, let us consider $(\bar{Y}_t^K)_{t \geq 0}$ a constrained overdamped Langevin process solution to the stochastic differential equation (19) with $p = dM + 1$, $q = N + 1$, and where for all $\bar{X} = (a, X) \in \mathbb{R} \times (\mathbb{R}^d)^M$, $\bar{V}(\bar{X}) = f(a)c(X)$ and $\bar{\Gamma}(\bar{X}) = (f(a) - 1, f(a)\varphi_1(X) - \mu_1, \dots, f(a)\varphi_N(X) - \mu_N)$. Then, the stochastic dynamics (19) can be viewed as a randomized version of a constrained gradient numerical method for the resolution of the optimization problem

$$\inf_{(A, Y) \in \mathcal{V}_K^N} \sum_{k=1}^K f(a_k) c(X^k), \quad (25)$$

where

$$\mathcal{V}_K^N := \left\{ (A, Y) \in \mathbb{R}^K \times \left((\mathbb{R}^d)^M \right)^K, \quad A = (a_k)_{1 \leq k \leq K}, \quad Y = (X^k)_{1 \leq k \leq K}, \right. \\ \left. \sum_{k=1}^K f(a_k) = 1, \quad \sum_{k=1}^K f(a_k) \vartheta(X^k) \leq A, \quad \forall 1 \leq n \leq N, \quad \sum_{k=1}^K f(a_k) \varphi_n(X^k) = \mu_n \right\}, \quad (26)$$

which is equivalent to problem (MCOT^K) using the surjectivity of f .

Note that the choice of the function f can influence the dynamics as it regulates both the way the brownian motion W affects the weights, and the balance, in the minimization of \bar{V} and in the enforcement of the constraint $\bar{\Gamma}(\bar{X}) = 0_N$, between a displacement of particles and a change in weights.

Here again, it is not clear in general that \bar{V} and $\bar{\Gamma}$ satisfies the regularity assumptions which ensures the convergence results stated in Section 3.1.2 to hold true. But, using formal computations, we can consider the associated measure $\bar{\pi}_\beta^a \in \mathcal{P}(\mathbb{R} \times (\mathbb{R}^d)^M)$ solution to

$$\bar{\pi}_\beta^a := \arg \min_{\substack{\bar{\pi} \in \mathcal{P}(\mathbb{R} \times (\mathbb{R}^d)^M) \\ \int_{a \in \mathbb{R}} \int_{X \in (\mathbb{R}^d)^M} f(a) d\bar{\pi}(a, X) = 1 \\ \forall 1 \leq n \leq N, \int_{a \in \mathbb{R}} \int_{X \in (\mathbb{R}^d)^M} f(a) \varphi_n(X) d\bar{\pi}(a, X) = \mu_n}} \bar{\mathcal{J}}(\bar{\pi}), \quad (27)$$

where

$$\bar{\mathcal{J}}(\bar{\pi}) := \int_{a \in \mathbb{R}} \int_{X \in (\mathbb{R}^d)^M} f(a) c(X) d\bar{\pi}(a, X) + \frac{\beta^2}{2} \int_{a \in \mathbb{R}} \int_{X \in (\mathbb{R}^d)^M} \ln \left(\frac{d\bar{\pi}(a, X)}{dadX} \right) d\bar{\pi}(a, X).$$

Let us introduce now $\pi_\beta^a \in \mathcal{P}((\mathbb{R}^d)^M)$ defined by

$$d\pi_\beta^a(X) = \int_{a \in \mathbb{R}} f(a) d\bar{\pi}_\beta^a(a, X).$$

Then π_β^a satisfies the constraints of problem (24) and

$$\bar{\mathcal{J}}(\bar{\pi}_\beta^a) = \int_{X \in (\mathbb{R}^d)^M} c(X) d\pi_\beta^a(X) + \frac{\beta^2}{2} \int_{a \in \mathbb{R}} \int_{X \in (\mathbb{R}^d)^M} \ln \left(\frac{d\bar{\pi}_\beta^a(a, X)}{dadX} \right) d\bar{\pi}_\beta^a(a, X).$$

Notice that, as a consequence, problem (27) may be seen as a second kind of entropic regularization of (MCOT) and that π_β^a is expected to be an approximation of some minimizer to (MCOT) as β goes to 0.

Let us notice here that the assumption made on f ensures that, for all $\pi \in \mathcal{P}((\mathbb{R}^d)^M)$, there exists a probability measure $\bar{\pi} \in \mathcal{P}(\mathbb{R} \times (\mathbb{R}^d)^M)$ such that

$$d\pi(X) = \int_{a \in \mathbb{R}} f(a) d\bar{\pi}(a, X).$$

Indeed, defining $d\bar{\pi}(a, X) := \mathbb{1}_I(a) da \otimes d\pi(X)$ yields the desired result. Besides, we easily check that $\bar{\mathcal{J}}(\bar{\pi}) = \mathcal{J}(\pi)$, which leads immediately to $\bar{\mathcal{J}}(\bar{\pi}_\beta^a) \leq \mathcal{J}(\pi_\beta^*)$ from the optimality of $\bar{\pi}_\beta^a$.

4 Numerical optimization method

We present in this section the numerical procedure we use in our numerical tests to compute approximate solutions to the particle problems with fixed weights (MCOT^K -fixed weight) or adaptive weights (MCOT^K) for a fixed given $K \in \mathbb{N}^*$. Note that (MCOT^K -fixed weight) can be equivalently rewritten as

$$J_K^N := \inf_{\substack{Y^K \in ((\mathbb{R}^d)^M)^K, \\ \Gamma^K(Y^K) = 0, \\ \Theta^K(Y^K) \leq A}} V^K(Y^K), \quad (28)$$

where V^K and Γ^K are defined in Section 3.2.1, and where

$$\Theta^K : \begin{cases} ((\mathbb{R}^d)^M)^K & \mapsto \mathbb{R} \\ Y := (X^1, \dots, X^K) & \rightarrow \frac{1}{K} \sum_{k=1}^K \vartheta(X^k). \end{cases}$$

Besides, problem (MCOT^K) can be rewritten equivalently as

$$I_K^N := \inf_{\substack{\bar{Y}^K \in (\mathbb{R} \times ((\mathbb{R}^d)^M))^K \\ \bar{\Gamma}^K(\bar{Y}^K) = 0, \\ \bar{\Theta}^K(\bar{Y}^K) \leq A}} \bar{V}^K(\bar{Y}^K), \quad (29)$$

where \bar{V}^K and $\bar{\Gamma}^K$ are defined in Section 3.2.2, and where

$$\bar{\Theta}^K : \begin{cases} (\mathbb{R} \times (\mathbb{R}^d)^M)^K & \mapsto \mathbb{R} \\ \bar{Y} := ((a^1, X^1), \dots, (a^K, X^K)) & \rightarrow \frac{1}{K} \sum_{k=1}^K f(a^k) \vartheta(X^k). \end{cases}$$

For the sake of simplicity, we restrict the presentation here to the method used for the resolution of (28), since the method used for the resolution of (29) follows exactly the same lines.

4.1 Time-discretization of constrained overdamped Langevin dynamics

The numerical procedure considered in this paper consists in a time discretization of the dynamics (14) with an adaptive time step and noise level. The main idea of the algorithm is the following: let $(W_n)_{n \in \mathbb{N}}$ be a sequence of iid normal vectors of dimension dMK . At each iteration $n \in \mathbb{N}^*$ of the procedure, starting from an initial guess $Y_0^K \in \mathcal{M}^K$ for $n = 0$, a new approximation $Y_{n+1}^K \in \mathcal{M}^K$ is computed as the projection in some sense of $Y_{n+1/2}^K := Y_n^K - \nabla V^K(Y_n^K) \Delta t_n + \beta_n \sqrt{\Delta t_n} W_n$ onto \mathcal{M}^K , where $\Delta t_n > 0$ is the time step and $\beta_n > 0$ is the noise level at iteration n . Precisely, the next iterate Y_{n+1}^K is computed as $Y_{n+1/2}^K + \nabla \Gamma^K(Y_n^K) \cdot \Lambda_{n+1}^K$ where $\Lambda_{n+1}^K \in \mathbb{R}^N$ is a Lagrange multiplier which ensures that the constraint $\Gamma^K(Y_{n+1}^K) = 0$ is satisfied.

The complete resulting procedure is summarized in Algorithm 1.

Algorithm 1 Constrained Overdamped Langevin Algorithm

Input $Y_0^K \in \mathcal{M}^K$, $\Delta t_0 > 0$, $\beta_0 > 0$, $\tau_0 > 0$, $i_{\text{const}} \in \mathbb{N}^*$, $i_{\text{max}} \in \mathbb{N}^*$, NoiseDecrease : $\mathbb{R}^+ \times \mathbb{N} \rightarrow \mathbb{R}^+$, $n_{\text{max}} \in \mathbb{N}^*$
 Fix $n = 0$, $\Lambda_0^K = 0$.
 Define $(W_n)_{n \in \mathbb{N}}$ a sequence of i.i.d. normal vectors of the same dimension as Y_0^K .
while $n \leq n_{\text{max}}$ **do**
 AdaptTimeStep($Y_n^K, \Lambda_n^K, \Delta t_n, \beta_n, \tau_n$)
 $Y_{n+1/2}^K := Y_n^K - \nabla V^K(Y_n^K) \Delta t_n + \beta_n \sqrt{\Delta t_n} W_n$
 if Projection($Y_{n+1/2}^K, \nabla \Gamma^K(Y_n^K), \Lambda_n^K, i_{\text{max}}$) succeeds **then**
 $Y_{n+1}^K, \Lambda_{n+1}^K, i_n \leftarrow$ Projection($Y_{n+1/2}^K, \nabla \Gamma^K(Y_n^K), \Lambda_n^K, i_{\text{max}}$)
 if $i_n \leq i_{\text{const}}$ **then**
 $\tau_{n+1} \leftarrow 2\tau_n$
 end if
 $\beta_{n+1} \leftarrow$ NoiseDecrease(β_n, n)
 $\Delta t_{n+1} \leftarrow \Delta t_n$; $\tau_{n+1} \leftarrow \tau_n$
 $n \leftarrow n + 1$
 else
 $\tau_n \leftarrow \tau_n / 2$
 end if
end while
return $\min(V^K(Y_n^K), 0 \leq n \leq n_{\text{max}})$

We discuss here three main difficulties about the algorithm we propose:

- the initialization step which consists in finding an element $Y_0^K \in \mathcal{M}^K$;
- the choice of the values of the time step Δt_n and noise level β_n at each iteration of the algorithm;
- the practical method used in order to compute a projection of $Y_{n+1/2}^K$ onto the submanifold \mathcal{M}^K , and in particular the value of the Lagrange multiplier Λ_{n+1}^K .

The procedure chosen to adapt the time step and noise level is discussed in Section 4.2. The algorithm used to compute a projection of $Y_{n+1/2}^K$ onto the submanifold \mathcal{M}^K and the value of the

Lagrange multiplier Λ_{n+1}^K is detailed in Section 4.3. Finally, the initialization procedure used to compute a starting guess $Y_0^K \in \mathcal{M}^K$ is explained in Section 4.4.

4.2 Time step and noise level adaptation procedure

Two remarks are in order to motivate the procedure we propose here:

- (i) the computation of the Lagrange multiplier Λ_{n+1}^K at each iteration n of the algorithm and of the resulting value of Y_{n+1}^K must be fast (as it is executed at each step).
- (ii) the time-step Δt_n must be:
 - (a) small enough for the procedure that computes the Lagrange multiplier to be well-defined,
 - (b) large enough for the total number of iterations needed to observe convergence to be reasonable. In practice, n_{\max} was chosen to be of the order of 20000 in the numerical experiments presented in Section 5.

To address item (i), we use a Newton method similar to the one proposed in [29, 30] to enforce the constraints and compute the Lagrange multiplier Λ_{n+1}^K which is summarized in Algorithm 3 and detailed in Section 4.3. This method is observed to converge fast if the value $Y_{n+1/2}^K$ is close enough to the submanifold \mathcal{M}^K . The tolerance threshold allowed at each step on the satisfiability of the constraints is given by $\tau_n > 0$, the value of which is also adapted at each step. Its precise value is inferred as follows: if the Newton method converges fast enough (i.e. if the number of iterations needed to ensure convergence i_n is lower than some fixed value i_{const}), then the value of τ_n is multiplied by 2. On the other hand, if the Newton method does not converge in a maximum number of iterations (given by i_{\max}), then τ_n is divided by 2. This step may involve a new time-step computation for iteration n , which we detail below.

The time-step Δt_n is adapted (in order to answer item (ii)) through the AdaptTimeStep subprocedure (Algorithm 2). It is increased at each step n if the constraints are satisfied up to a tolerance threshold *lower* than τ_n (in order to answer (iib)). Otherwise, the time-step is divided by 2 as many times as needed for $Y_{n+1/2}^K$ to satisfy the constraints defining the submanifold up to a tolerance lower than τ_n (in order to satisfy item (iia)).

Moreover, the noise-level β_n is decreased at each iteration n at a rate inspired from Robbins-Siegmund Lemma [36, Theorem 6.1] for non-constrained stochastic gradient optimization, using the NoiseDecrease function in Algorithm 1. This is managed through the NoiseDecrease function. In the numerical experiments presented in Section 5, we used two possible choices of NoiseDecrease function defined respectively by $(\beta, n) \mapsto \beta$ (noise level unchanged) and $(\beta, n) \mapsto \sqrt{\frac{n}{n+1}}\beta$ (slow decrease of the noise level: note that this is the relative decrease, so that after n steps, the noise is $\beta_0/\sqrt{1+n}$).

Algorithm 2 AdaptTimeStep subprocedure

```

Input:  $Y^K, \Lambda, \Delta t, \beta, \tau, n$ 
if  $\|\Gamma^K(Y^K - \nabla V^K(Y^K)2\Delta t + W_n\sqrt{2\Delta t}\beta)\| \leq \tau$  then
   $\Delta t \leftarrow 2\Delta t$ ;
else
  while  $\|\Gamma^K(Y^K - \nabla V^K(Y^K)\Delta t + W_n\sqrt{2\Delta t}\beta)\| \geq \tau$  do
     $\Delta t \leftarrow \Delta t/2$ ;  $\Lambda \leftarrow \Lambda/2$ 
  end while
end if

```

4.3 Projection method

As mentioned earlier, to compute $Y_{n+1}^K \in \mathcal{M}^K$ and Λ_{n+1}^K from $Y_{n+1/2}^K$, we use a Newton method similar to the one proposed in [29, 30]. We refer the reader to [30, Section 2.2.2] for theoretical considerations on such projections.

More precisely, the procedure reads as follows: given $Y_n^K, Y_{n+1/2}^K \in ((\mathbb{R}^d)^M)^K$, the aim of the Newton procedure is to find a solution $\Lambda_{n+1}^K \in \mathbb{R}^N$ to the equation

$$\Gamma^K \left(Y_{n+1/2}^K + \nabla \Gamma^K(Y_n^K) \cdot \Lambda_{n+1}^K \right) = 0.$$

We numerically observe that this Newton procedure only converges in cases when $Y_{n+1/2}^K$ and Y_n^K are close enough to the manifold \mathcal{M}^K . Provided that Y_n^K belongs to \mathcal{M}^K , $Y_{n+1/2}^K$ can be made arbitrarily close to the submanifold provided that the value of the time step Δt_n is chosen small enough. We also refer the reader to [40, Theorem 1.4.1] for theoretical conditions which guarantee the convergence of this Newton procedure.

This projection procedure, together with the routine for the adaptation of the error tolerance τ_n on the satisfiability of the constraints, is summarized in Algorithm 3. Note that this Newton algorithm requires the inversion of matrices of the form

$$\nabla \Gamma^K(Y_{n+1/2}^K + \nabla \Gamma^K(Y_n^K) \cdot \Lambda)^T \cdot \nabla \Gamma(Y_n^K)$$

for $\Lambda \in \mathbb{R}^N$ and that we cannot theoretically guarantee the invertibility of this matrix in general. In practice, it naturally depends significantly on the choice of test functions $(\phi_n)_{1 \leq n \leq N}$.

Algorithm 3 Projection subprocedure (Newton method)

Input: $Y_{n+1/2}^K, \nabla \Gamma^K(Y_n^K), \Lambda_n^K, i_{\max}$
 $i = 0, \Lambda'_0 \leftarrow \Lambda_n$
while $\|\Gamma^K(Y_{n+1/2}^K + \nabla \Gamma^K(Y_n^K) \cdot \Lambda'_i)\| > 10^{-16}$ and $i \leq i_{\max}$ **do**
 $\Lambda'_{i+1} \leftarrow \Lambda'_i - \left(\nabla \Gamma^K(Y_{n+1/2}^K + \nabla \Gamma^K(Y_n^K) \cdot \Lambda'_i)^T \cdot \nabla \Gamma(Y_n^K) \right)^{-1} \cdot \Gamma^K(Y_{n+1/2}^K + \nabla \Gamma^K(Y_n^K) \cdot \Lambda'_i)$
 $i \leftarrow i + 1$
end while
if $\|\Gamma^K(Y_{n+1/2}^K + \nabla \Gamma^K(Y_n^K) \cdot \Lambda'_i)\| \leq 10^{-16}$ **then**
 return $Y_{n+1/2}^K + \nabla \Gamma^K(Y_n^K) \cdot \Lambda'_i, \Lambda'_i, i$
else
 return Projection failure.
end if

4.4 Initialization procedure

Algorithm 1 is initialized with an initial guess Y_0^K which is assumed to belong to the constraints submanifold \mathcal{M}^K . In practice, finding an element which belongs to this submanifold is a delicate task, especially when the number of test functions is large. Indeed, as mentioned in the preceding section, the Newton procedure described in Section 4.3 only converges if the starting point of the algorithm is sufficiently close to the manifold \mathcal{M}^K . This is the reason why this initialization step is rather performed using a method inspired from [49, Section 5 example 3]. A Runge-Kutta 3 (Bogacki-Shampine) numerical scheme [41, (5.8-42)] is used in order to discretize the dynamics

$$\frac{d}{dt} Y^K(t) = F(Y^K(t))$$

starting from a random initial state $Y^K(t=0) = Y^{K,0} \in ((\mathbb{R}^d)^M)^K$, where F is defined as

$$\forall Y^K \in ((\mathbb{R}^d)^M)^K, \quad F(Y^K) = - \|\Gamma^K(Y^K)\|_2^2 \frac{\nabla \Gamma^K(Y^K) \cdot \Gamma^K(Y^K)}{\|\nabla \Gamma^K(Y^K) \cdot \Gamma^K(Y^K)\|_2^2}. \quad (30)$$

We observe that such a numerical procedure is more robust than a Newton algorithm, even if it can converge very slowly.

Let us mention here that, in the case of the particle problem (29) with adaptive weights, an additional step may be used prior to such a Runge-Kutta method, which consists in using a Carathéodory-Tchakaloff subsampling procedure. Carathéodory-Tchakaloff subsampling [39, 45] has been introduced to compute low nodes cardinality cubatures.

In our context, this method can be adapted to find a low nodes cardinality starting point, as close as possible to the constraints submanifold $\overline{\mathcal{M}}^K$. More precisely, the method works as follows: we fix a value $K_\infty \gg K$ and compute $(X^1, \dots, X^{K_\infty})$ iid samples of random vectors according to the probability law μ . A Non-Negative Least Squares (NNLS) is then used to find a sparse solution to the optimization problem

$$w^* \in \arg \min_{w \in \mathbb{R}_+^{K_\infty}} \|\Phi w - \bar{\mu}\|^2, \quad (31)$$

where $\Phi := (\Phi_{n,k})_{1 \leq n \leq N+1, 1 \leq k \leq K_\infty} \in \mathbb{R}^{N \times K_\infty}$, $\bar{\mu} = (\mu_1, \dots, \mu_N, 1) \in \mathbb{R}^{N+1}$ and

$$\forall 1 \leq k \leq K_\infty, \quad \forall 1 \leq n \leq N, \quad \Phi_{n,k} = \varphi_n(X^k) \text{ and } \Phi_{N+1,k} = 1.$$

By Kuhn-Tucker conditions for the NNLS problem [26, Theorem (23.4)], there exists a solution $w^* := (w_k^*)_{1 \leq k \leq K_\infty} \in \mathbb{R}_+^{K_\infty}$ to (31) such that $\#J \leq N+1$ with $J := \{1 \leq k \leq K_\infty, w_k^* > 0\}$. Common algorithms such as the Lawson-Hanson method [26, Theorem (23.10)] enable to compute such a sparse solution. Let us point out that any solution w^* to (31) then satisfies

$$\sum_{n=1}^N \left| \sum_{k \in J} w_k^* \varphi_n(X^k) - \bar{\mu}_n \right|^2 \leq \sum_{n=1}^N \left| \frac{1}{K_\infty} \sum_{k=1}^{K_\infty} \varphi_n(X^k) - \bar{\mu}_n \right|^2. \quad (32)$$

In practice, in the case when $\#J \leq K$, the positions and weights returned by the Carathéodory-Tchakaloff Subsampling procedure are subdivided and randomly perturbed with a small amount of noise.

5 Numerical tests

The aim of this section is to illustrate the results obtained via the numerical procedure described in Section 4 for the resolution of the particle problems (29) and (28) in different test cases.

Section 5.1 is devoted to results obtained in cases where $d = 1$ and Section 5.2 contains numerical results obtained in examples where $d = 3$. The experiments presented in this section have been implemented in python 3 using scipy and numpy modules, and tested on a server with an Intel Xeon processor with 32 cores (hyperthreaded) and 192 Go RAM.

5.1 One-dimensional test cases ($d = 1$)

5.1.1 Theoretical elements

In the case where $d = 1$, the solution to the optimal transport problem (2) is analytically known in the case when c is a symmetric repulsive cost from [12, Theorem 1.1]. For sake of completeness, we recall their result for the cost function that we consider in our numerical experiments.

Theorem 3 (Colombo, De Pascale, Di Marino, 2015). *Let $\epsilon \geq 0$ and $c : \mathbb{R}^M \rightarrow [0, +\infty]$ be the cost defined by*

$$\forall x_1, \dots, x_M \in \mathbb{R}, \quad c(x_1, \dots, x_M) = \sum_{1 \leq i, j \leq M, i \neq j} \frac{1}{\epsilon + |x_i - x_j|}. \quad (33)$$

Let μ be an non atomic probability measure on \mathbb{R} such that

$$\min_{\pi \in \Pi(\mu; M)} \int_{\mathbb{R}^M} c(x_1, \dots, x_M) d\pi(x_1, \dots, x_M) < +\infty. \quad (34)$$

Let $-\infty = d_0 < d_1 < \dots < d_M = +\infty$ be such that

$$\mu([d_i, d_{i+1}]) = \frac{1}{M}, \quad i = 0, \dots, M - 1. \quad (35)$$

Let $T : \mathbb{R} \rightarrow \mathbb{R}$ be the unique (up to μ -null sets) function increasing on each interval $[d_i, d_{i+1}]$, $i = 0, \dots, M - 1$ and such that

$$\begin{aligned} T\#(\mathbf{1}_{[d_i, d_{i+1}]} \mu) &= \mathbf{1}_{[d_{i+1}, d_{i+2}]} \mu, \quad i = 0, \dots, M - 2 \\ T\#(\mathbf{1}_{[d_{M-1}, d_M]} \mu) &= \mathbf{1}_{[d_0, d_1]} \mu. \end{aligned} \quad (36)$$

Then T is an admissible map for

$$\inf_{T: \mathbb{R} \rightarrow \mathbb{R} \text{ Borel}, T\#\mu = \mu, T^{(M)} = \text{Id}} \int_{\mathbb{R}} c(x, T(x), \dots, T^{(M-1)}(x)) d\mu(x), \quad (37)$$

where $T^{(i)} = \overbrace{T \circ \dots \circ T}^{i \text{ times}}$.

Moreover, the only symmetric optimal transport plan is the symmetrization of the plan induced by the map T .

We make use of Theorem 3 to compare the exact solution of problem (2) together with the approximation given by the numerical procedure described in Section 4 to solve the MCOT particle problems with fixed or adaptive weights.

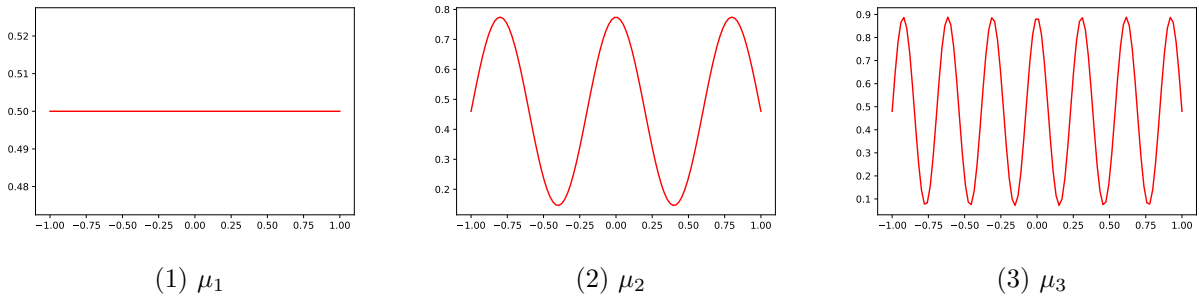


Figure 1: Densities of the marginal laws tested for 1D numerical tests.

5.1.2 Marginals, test functions, cost and weight functions

Marginals. The numerical experiments in this section were realized with three different marginal laws, which are respectively denoted by μ_1 , μ_2 and μ_3 and defined by

$$d\mu_1(x) := \frac{1}{2} \mathbf{1}_{[-1,1]}(x) dx, \quad (38)$$

$$d\mu_2(x) := \left[\frac{\pi}{10} \cos\left(\frac{5\pi}{2}x\right) + 0.46 \right] \mathbf{1}_{[-1,1]}(x) dx, \quad (39)$$

$$d\mu_3(x) := \left[0.13\pi \cos\left(\frac{13\pi}{2}x\right) + 0.48 \right] \mathbf{1}_{[-1,1]}(x) dx. \quad (40)$$

The densities of μ_1, μ_2, μ_3 are plotted in Figure 1.

Test functions. The test functions $(\phi_n)_{1 \leq n \leq N}$ used are Legendre Polynomials with the following scaling

$$\phi_n = \frac{\sqrt{2n + \frac{1}{2}}}{n + 1} P_n, \quad (41)$$

where P_n is the Legendre Polynomial of degree n . As the marginal laws considered have their support in $[-1, 1]$, we chose the Legendre polynomials for their orthogonality property. Besides, by using polynomials, the matrix $\nabla\Gamma(X)$ is related to a Vandermonde matrix, the invertibility of which (crucial to enforce the constraints by Algorithm 3 or the Runge-Kutta method) is ensured as long as particles are spread on more than N locations.

Cost. We use in all experiments the regularized Coulomb cost function (33) with $\epsilon = 10^{-1}$.

Weight functions. Two different choices of weight functions f are studied in the numerical experiments presented below: the squared weight function $f : \mathbb{R} \ni a \mapsto a^2$ and the exponential weight function $f : \mathbb{R} \ni a \mapsto e^{-a}$. Although we do not have strong criteria to choose a weight function, the intuition behind the squared weight function is that it can behave well regarding the enforcement of the constraints by a Newton method, given that $\bar{\Gamma}$ is then a polynomial. The intuition behind the exponential weight function is that it could slow down the cancellation of the weights of the particles, keeping alive more degrees of freedom for the optimization process.

5.1.3 Initialization step – Figure 2

The aim of Figure 2 is to plot the decrease of $\|\Gamma^K(Y_m^K)\|_\infty$ as a function of the number of iterations of the Runge-Kutta 3 method presented in Section 4.4, in a test case where $M = 5$. We numerically observe here that, as expected, as N increases, the number of iterations needed by the Runge-Kutta

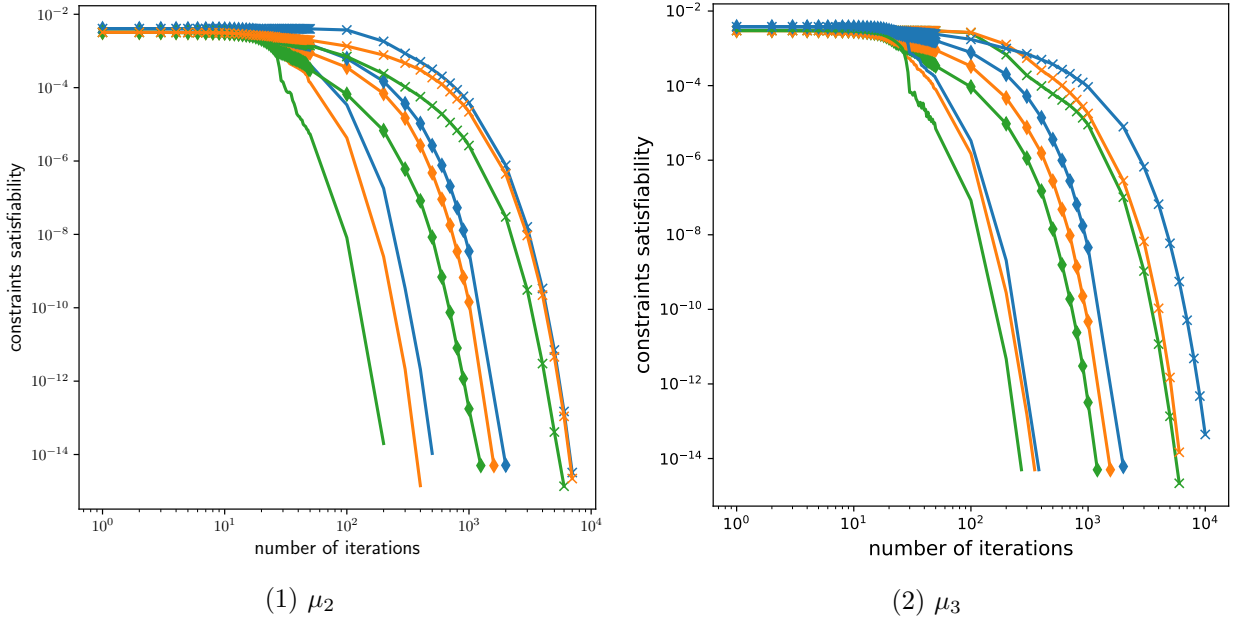


Figure 2: Evolution of $\|\Gamma^K(Y_m^K)\|_\infty$ for different weight functions as a function of the number of iterations m of the Runge-Kutta 3 procedure. Tests were performed with $M = 5$, $K = 10000$. Blue curves uses fixed weights, orange curves uses an exponential weight function and green curves a squared weight function. No marker is for $N = 10$, a diamond marker for $N = 20$ and a “+” marker for $N = 40$. Caratheodory-Tchakaloff subsampling gave initial values of 1.11×10^{-16} (3.83×10^{-16} , 3.02×10^{-16}) for μ_2 , $N = 10$ (resp. $N = 20$, $N = 40$) and 3.33×10^{-16} (1.28×10^{-16} , 4.66×10^{-16}) for μ_3 , $N = 10$ (resp. $N = 20$, $N = 40$).

procedure to reach convergence increases. Besides, we observe that the additional degrees of freedom of the cases using weight functions allow a faster initial optimization – yet not heavily pronounced, as well as an initialization slightly faster for the squared weight function compared to the exponential one.

5.1.4 Decrease of the cost function – Figures 3, 4 and 5

The aim of Figures 3, 4 and 5 is to plot the evolution of $V^K(Y_n^K)$ (or $\bar{V}^K(\bar{Y}_n^K)$) as a function of n the number of iterations of the constrained overdamped Langevin algorithm presented in Section 4 for various values of N , various weight functions, values of β_0 and NoiseDecrease functions, and using or not a subsampling at initialization. We observe in Figure 3 that decreasing the noise as the squareroot of the number of iterations n converges faster than keeping it constant, and that keeping $\beta_0 = 0$ is the fastest. In Figure 4 we remark that the higher N the slower the optimization (with the particular case of μ_3 , $N = 20$ with the squared weight function which does not converge in 20000 iterations), and that cases initialized by Caratheodory-Tchakaloff subsampling tend to start with a higher cost. In Figure 5, we observe that with $K = 10000$ particles, considering fixed or variable weights does not strongly change the speed of convergence (but for the case μ_3 , $N = 20$ with the squared weight function mentioned above). However, using variable weights with $K = 100$ particles seems to be the fastest set of parameters.

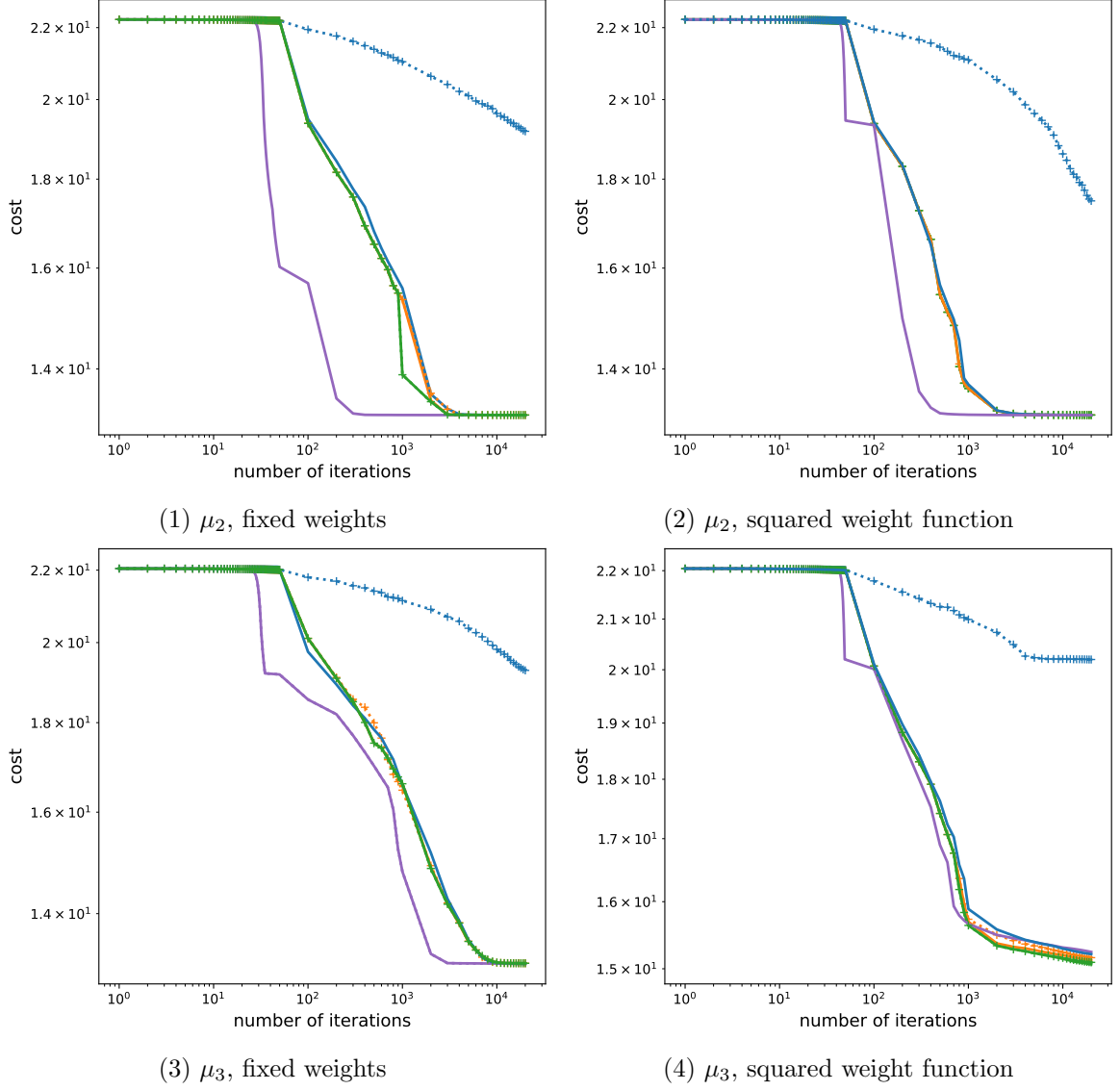


Figure 3: Evolution of the cost as a function of the number of iterations n for various weight functions and values of β_0 , for μ_2 and μ_3 . Tests were performed with $M = 5$, $N = 20$, $K = 10000$ and $\Delta t_0 = 10^{-3}$. Blue curves are for $\beta_0 = 10^{-1.5}$, orange curves for $10^{-3.5}$, green curves for $10^{-5.5}$ and purple curves for $\beta_0 = 0$. Solid lines have a decrease of the noise in the squareroot of time whereas dotted lines with a “+” marker have no decrease of the noise.

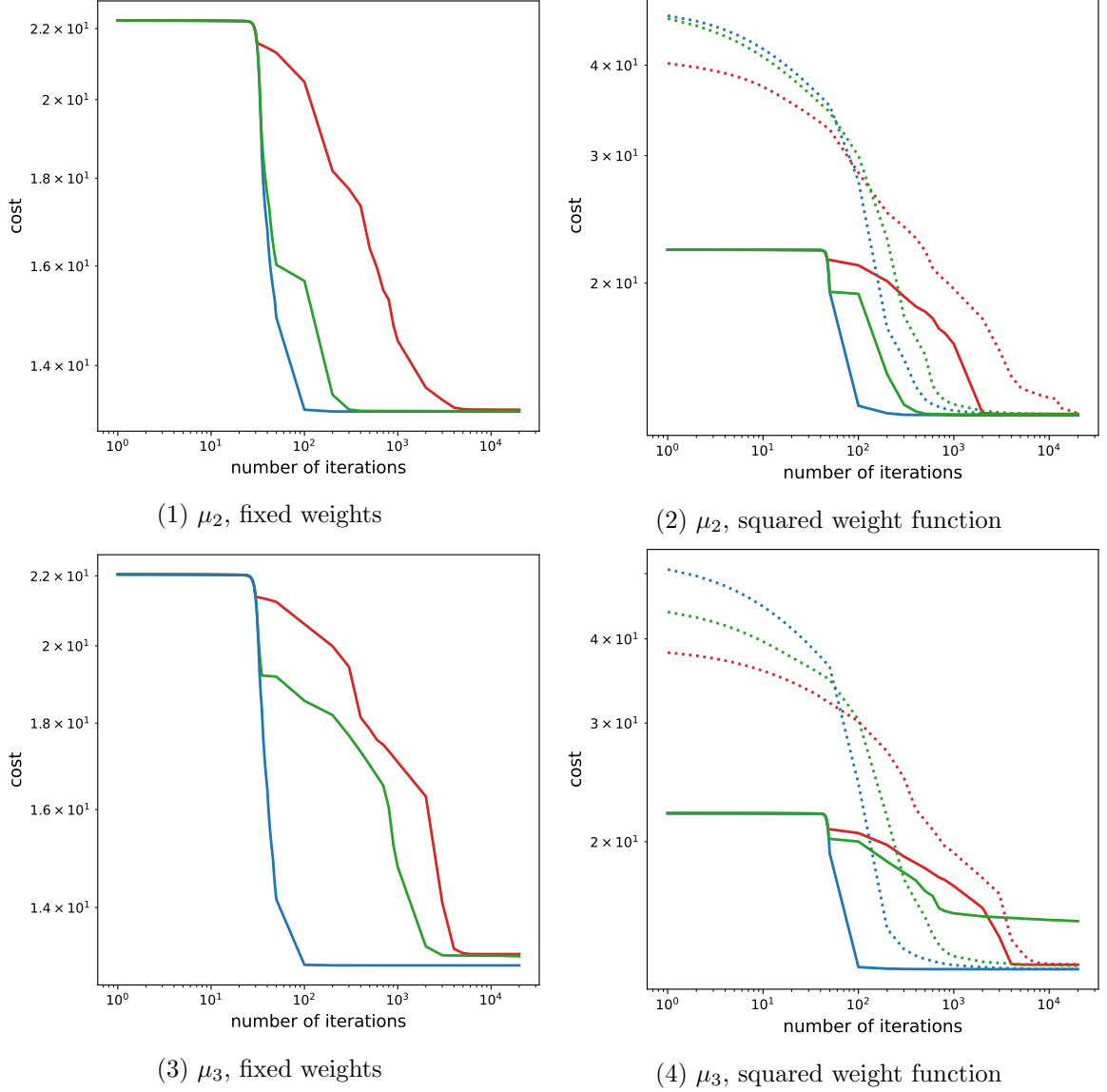


Figure 4: Evolution of the cost as a function of the number of iterations n for various weight functions and values of N , for μ_2 and μ_3 . Tests were performed with $M = 5$, $\beta_0 = 0$, $K = 10000$ and $\Delta t_0 = 10^{-3}$. Blue curves for $N = 10$, green curves for $N = 20$ and red curves for $N = 40$. Dotted lines correspond to tests initialized by Caratheodory-Tchakaloff subsampling whereas tests solid lines correspond to tests initialized by Runge-Kutta 3 method.

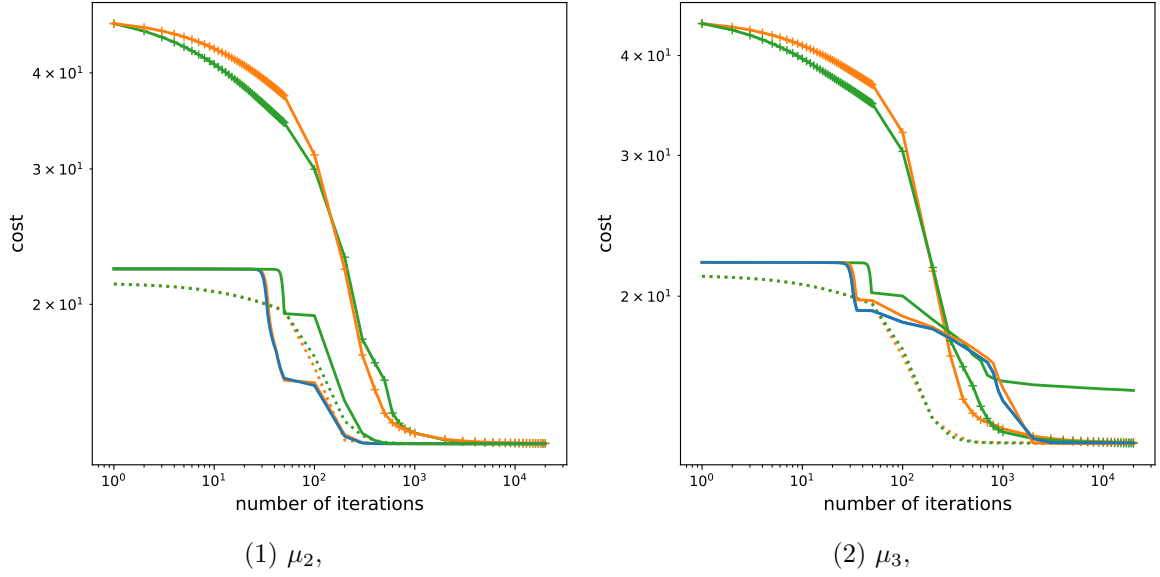


Figure 5: Evolution of the cost as a function of the number of iterations n for various weight functions, for μ_2 and μ_3 . Tests were performed with $M = 5$, $N = 20$, $\beta_0 = 0$ and $\Delta t_0 = 10^{-3}$. Blue curves uses fixed weights, orange curves uses an exponential weight function and green curves a squared weight function. $K = 10000$ particles for solid lines and $K = 100$ particles for dotted lines. Optimization following a Caratheodory-Tchakaloff subsampling at initialization uses “+” markers.

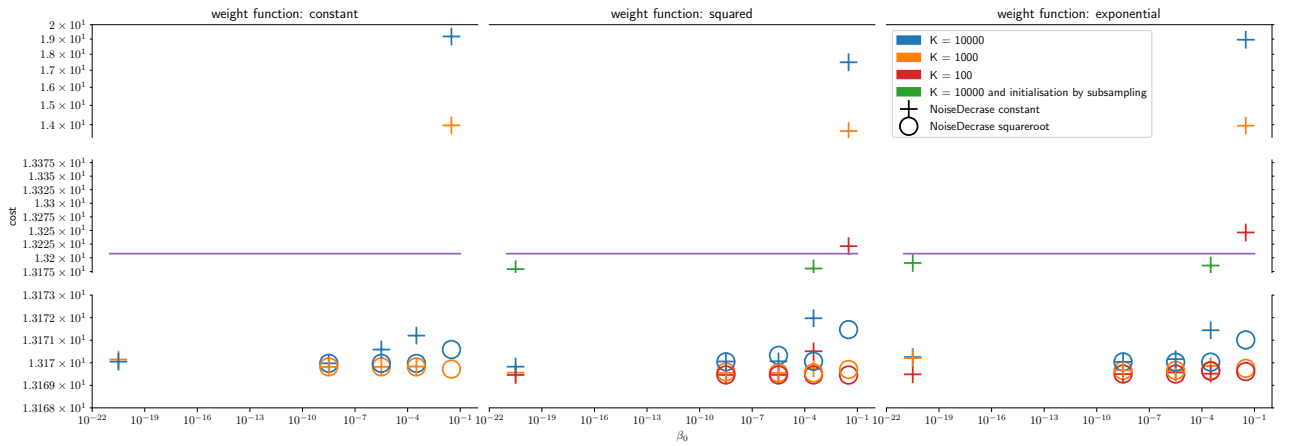


Figure 6: Lowest cost value reached during optimization by the constrained overdamped Langevin algorithm in function of the β_0 , for various weight functions, values of K and choices of NoiseDecrease functions. The purple line corresponds to the optimal transport cost. The marginal law is μ_2 , $N = 20$, $M = 5$, $\Delta t_0 = 10^{-3}$.

5.1.5 Minimal values of cost – Figure 6

The goal of Figure 6 is to compare the minimal values of the cost obtained by the algorithm for different parameters together with its analytic value. We observe that considering adaptive weights enable to reach lower optimal costs than with fixed weights, but the relative difference between the approximate minimal cost values is lower than 0.1%. When the noise level decreases in the square root of the number of iterations a lower optimal cost can be reached compared to a constant noise level. In the variable weights cases, the lower K the lower the optimal cost, but when the optimization starts with a Tchakaloff subsampling solution, for which the lowest cost reached is 0.3% higher than with the Runge-Kutta 3 method.

5.1.6 Optimal position of particles – Figures 7, 8 and 9

The aim of Figures 7, 8 and 9 is to plot the positions of the particles obtained by the numerical procedure presented in Section 4 for respectively μ_1 , μ_2 and μ_3 and different values of K , N , β_0 , initialization methods, and in fixed and variable weights cases. We numerically observe that the obtained particles are located close to the support of the exact optimal transport plan, and that the higher the value of N the more precise the approximation of this transport map is [1, Theorem 4.1]. Also, when $K = 10000$ and even more when $\beta_0 = 10^{3.5}$, particles are more spreaded around the transport map.

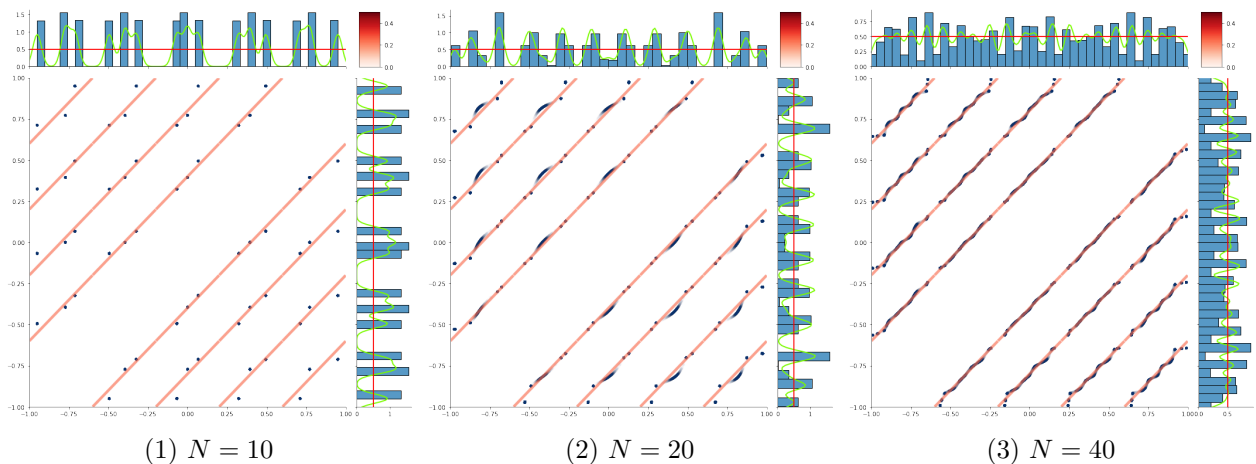


Figure 7: Optimal transport with μ_1 and $M = 5$, $\Delta t_0 = 10^{-3}$. In each plot, on the main graph $\frac{1}{M(M-1)} \sum_{k=1}^K \sum_{m \neq m'=1}^M w_k \delta_{x_m^k, x_{m'}^k}$ is represented by blue particles. The darker the heavier the particle. Particles have some transparency which allows to see more clearly areas of high concentration. Red curves represent the functions T^i for $i \in \{1, \dots, M-1\}$ defined in Theorem 3. The higher the density the darker. On side graphs are represented in blue a weighted histogram of the particles, in red the marginal law and in green a normal kernel density estimate based on the weighted particles (with a bandwidth rule based on Scott's rule with $d = 0$).

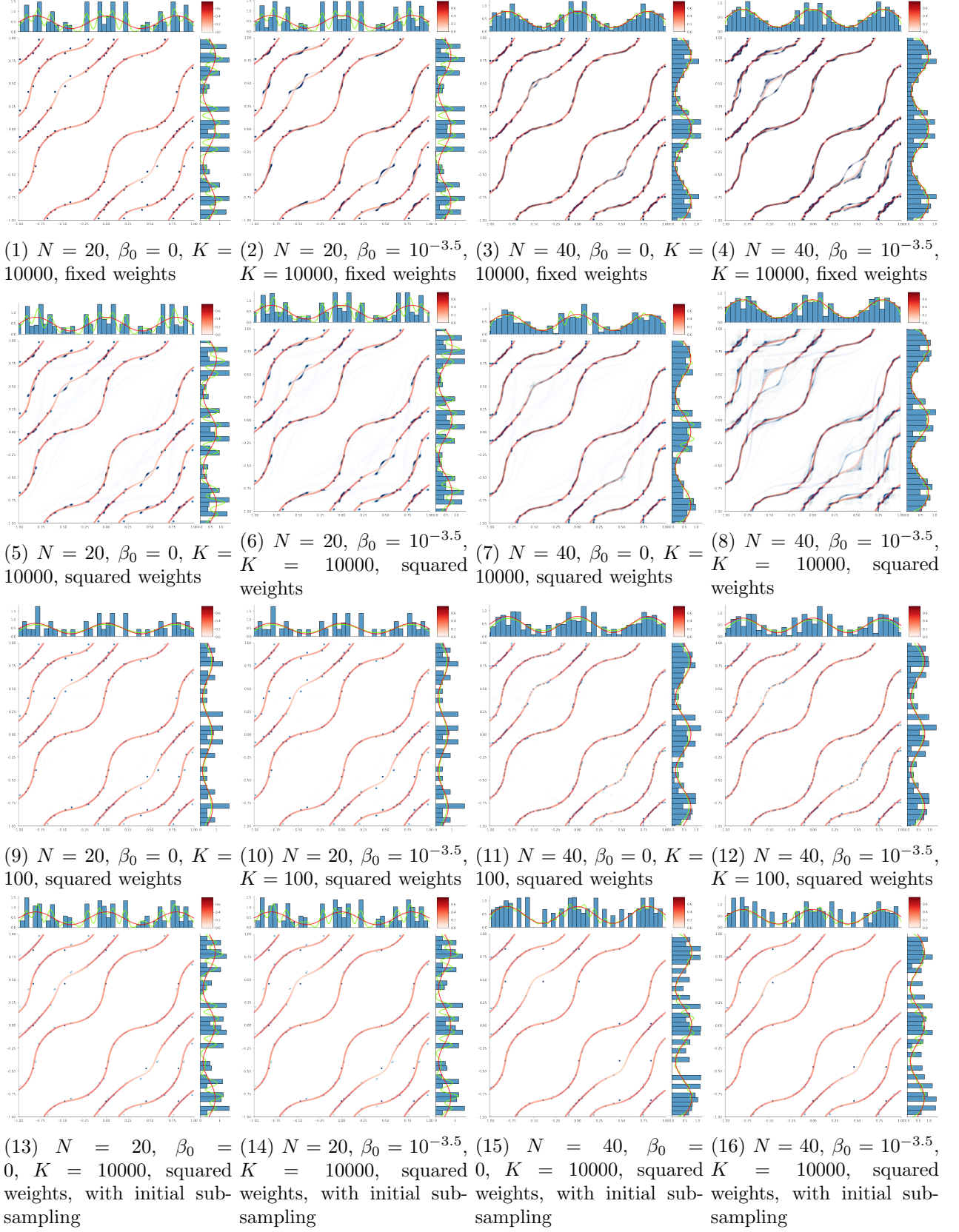


Figure 8: Optimal transport with μ_2 and $M = 5$, $\Delta t_0 = 10^{-3}$. In each plot, on the main graph $\frac{1}{M(M-1)} \sum_{k=1}^K \sum_{m \neq m'=1}^M w_k \delta_{x_{m^k}, x_{m'^k}}$ is represented by blue particles. The darker the heavier the particle. Particles have some transparency which allows to see more clearly areas of high concentration. Red curves represent the functions T^i for $i \in \{1, \dots, M-1\}$ defined in Theorem 3. The higher the density the darker. On side graphs are represented in blue a weighted histogram of the particles, in red the marginal law and in green a normal kernel density estimate based on the weighted particles (with a bandwidth rule based on Scott's rule with $d = 0$).

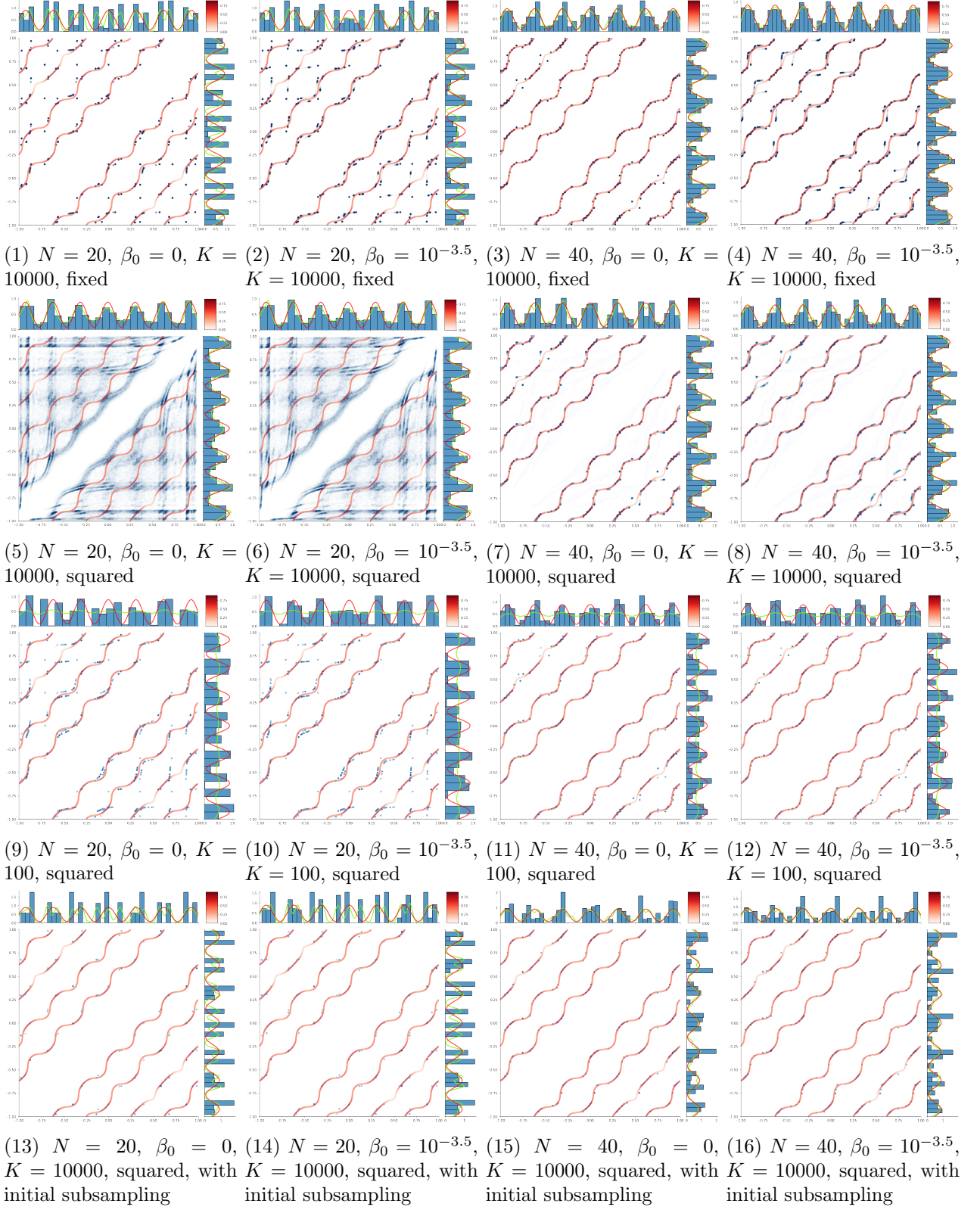


Figure 9: Optimal transport with μ_3 and $M = 5, \Delta t_0 = 10^{-3}$. In each plot, on the main graph $\frac{1}{M(M-1)} \sum_{k=1}^K \sum_{m \neq m'=1}^M w_k \delta_{x_m^k, x_{m'}^k}$ is represented by blue particles. The darker the heavier the particle. Particles have some transparency which allows to see more clearly areas of high concentration. Red curves represent the functions T^i for $i \in \{1, \dots, M-1\}$ defined in Theorem 3. The higher the density the darker. On side graphs are represented in blue a weighted histogram of the particles, in red the marginal law and in green a normal kernel density estimate based on the weighted particles (with a bandwidth rule based on Scott's rule with $d = 0$).

5.2 Three-dimensional test cases ($d = 3$)

5.2.1 Tests design

The numerical experiments were realized with four different marginal laws that are named afterwards as follows:

$$\mu_1 \sim \mathcal{N}(0_3, \text{Id}_3), \quad (42)$$

$$\mu_2 \sim \frac{2}{3}\mathcal{N}\left(0_3, \begin{pmatrix} 1 & 0.5 & 0.75 \\ 0.5 & 2 & 1.5 \\ 0.75 & 1.5 & 3 \end{pmatrix}\right) + \frac{1}{3}\mathcal{N}\left(\begin{pmatrix} 2 \\ 2 \\ 2 \end{pmatrix}, \begin{pmatrix} 1 & 0.8 & 0.22 \\ 0.8 & 2 & 1.8 \\ 0.22 & 1.8 & 3 \end{pmatrix}\right), \quad (43)$$

$$\begin{aligned} \mu_3 \sim & \frac{1}{10}\mathcal{N}(0_3, C) + \frac{1}{5}\mathcal{N}\left(\begin{pmatrix} 4 \\ 0 \\ 0 \end{pmatrix}, C\right) + \frac{1}{5}\mathcal{N}\left(\begin{pmatrix} 8 \\ 0 \\ 0 \end{pmatrix}, C\right) + \frac{1}{5}\mathcal{N}\left(\begin{pmatrix} 12 \\ 0 \\ 0 \end{pmatrix}, C\right) \\ & + \frac{1}{5}\mathcal{N}\left(\begin{pmatrix} 16 \\ 0 \\ 0 \end{pmatrix}, C\right) + \frac{1}{10}\mathcal{N}\left(\begin{pmatrix} 20 \\ 0 \\ 0 \end{pmatrix}, C\right), \quad \text{with } C = \begin{pmatrix} 1 & 0.5 & 0.75 \\ 0.5 & 2 & 1.5 \\ 0.75 & 1.5 & 3 \end{pmatrix}, \end{aligned} \quad (44)$$

$$\mu_4 \sim \mathcal{U}(\mathcal{B}(0, 1)). \quad (45)$$

And, for $i = 1, 2, 3, 4$, using as test functions^v tensor products of 1D orthonormal polynomials $(P_l^{\mu_i, j})_{\substack{1 \leq j \leq 3, \\ l \in \mathbb{N}}}$, defined as, for $j = 1, 2, 3$, $l \in \mathbb{N}$,

$$\text{degree}(P_l^{\mu_i, j}) = l, \quad \forall l' < l, \quad \int_{\mathbb{R}^3} P_l^{\mu_i, j}(x_j) P_{l'}^{\mu_i, j}(x_j) d\mu_i(x_1, x_2, x_3) = \frac{1}{(l+1)^2} \delta_{l, l'}. \quad (46)$$

As for a finite number of multivariate polynomials (and under a suitable control of mixed derivatives), the hyperbolic cross [15] seems to behave better than using all polynomials up to a given degree, we used, for a number of test functions N appropriately chosen, the polynomials $P_{l_1}^{\mu_i, 1} \otimes P_{l_2}^{\mu_i, 2} \otimes P_{l_3}^{\mu_i, 3}$, where

$$(l_1 + 1)(l_2 + 1)(l_3 + 1) \leq L_N, \quad (47)$$

where L_N is defined such that $\#\{(l_1, l_2, l_3) | (l_1 + 1)(l_2 + 1)(l_3 + 1) \leq L_N\} = N$. The map between maximum degree of the polynomials ($L_N - 1$) and N is shown in Table 1.

$L_N - 1$	6	7	8	9	10	11
N	28	38	44	53	56	74

Table 1: Map between the maximum degree of 1D polynomials and the number of test functions using hyperbolic cross in 3D.

In the numerical examples presented afterwards, as all weights are fixed to $\frac{1}{K}$, there is no need to use the polynomial of degrees $(l_1, l_2, l_3) = (0, 0, 0)$, hence values of N decreased by 1 compared to the values of Table 1.

Remark 4. *One of the main advantages of using sums of Normal functions (or a uniform measure on a ball) as marginal laws and polynomials as test functions is that their exists in that case close formulas for the computation of the moments. From our experiments in dimension 1, the precision of the computation of the moments is important both for the solution of the MCOT problem to be well-defined (and thus for the algorithm to converge) – numerically computed moments, though not*

^vThese polynomials were chosen after a few numerical tests on some optimization procedures for their better convergence properties than the polynomials they were compared to. Their tensorised form both eases the computation of the moments and allows some parallelisation. Note also that the matrix $\nabla \Gamma^K(Y^K)$ is a multivariate Vandermonde matrix. We checked numerically its invertibility throughout the optimization process.

exact, must allow the existence of $Y^K \in ((\mathbb{R}^d)^M)^K$ such that $\|\Gamma^K(Y^K)\|_\infty \leq \epsilon$ for ϵ the machine-precision; and for the convergence as N increases of the MCOT cost towards the OT cost – numerically computed moments not precise enough might hide this convergence. Numerical quadratures in 3D could be implemented for dealing with more general marginal laws and test functions, however, their computation and convergence speed put it beyond the scope of this article.

Mean-Covariance. Tests were also performed using as test functions the mean and covariance matrix for μ_1 and μ_2 , in order to notice on examples how much those test functions do constrain an optimal transport problem. Note that this problem of optimal transport when the mean and covariance structure are given may be interesting per se, when only partial information on the distribution is known. We have indicated in Table 2 the optimal costs obtained with our algorithm for μ_1 and μ_2 with mean-covariance constraints ($N = 9$) and with many moment constraints ($N = 52$). We observe on our examples a relative difference around 15-20%.

	$\mu_1, M = 10$	$\mu_1, M = 100$	$\mu_2, M = 10$	$\mu_2, M = 100$
$N = 9$	10.65	1395	8.007	1074
$N = 52$	12.50	1599	9.107	1201

Table 2: Optimal value of the cost obtained for μ_1 and μ_2 with mean-covariance constraints ($N = 9$) and with many moment constraints ($N = 52$).

Cost. In order to avoid too high values of the cost function, we used in all experiments a regularized Coulomb cost $c(x_1, \dots, x_M) = \sum_{m \neq m'=1}^M \frac{1}{\epsilon + |x_m - x_{m'}|}$, with $\epsilon = 10^{-3}$ and $\forall i = 1, \dots, M, x_m \in \mathbb{R}^3$.

Fixed weights. After several tests comparing fixed and variable weights (with various weight functions), we observe that in dimension 3, for the marginal laws considered, both initialization and optimization using variable weights were much slower than using fixed weights. Therefore, all following tests have been performed using fixed weights. Heuristically, when using variable weights, some particles tend to have large weights and are strongly constrained while other ones become lightweight and do not move much since the gradient on positions is proportional to weights.

5.2.2 Initialization and constraints enforcement – Figure 10

Initialization was performed by a sampling K particles according to the marginal law, and then using the Runge-Kutta method showed in Section 4.4 to bring the particles on the submanifold of the constraints \mathcal{M}^K . This method has been tested for various values of N and K , presented respectively in Figures 10.

As N increases (Figure 10), the submanifold of the constraints becomes harder to reach using the Runge-Kutta method (similarly to the 1D case), and large values of N ($L_N \geq 11$) could not be attained in the time of the numerical experiment (remind that the number of computations involved at each iteration grows linearly with N). In the case of each marginal laws (μ_1 and μ_2) for which the tests have been performed, despite the asymmetry of μ_2 , the dependence on N of the convergence speed appears to be similar.

Note also that as we use symmetrised test functions (regarding the marginal laws) with fixed weights, the number of independant coordinates involved in the Runge-Kutta method to satisfy the constraints is linear in KM (M being the number of marginal laws). Thus, solving the problem of finding a starting point on the submanifold with 100 marginal laws and 10^3 particles is numerically the same as the one with 10 marginal laws and 10^4 particles. Although in the case where weights are variable this remark can not be applied, as coordinates on different marginal laws of the same

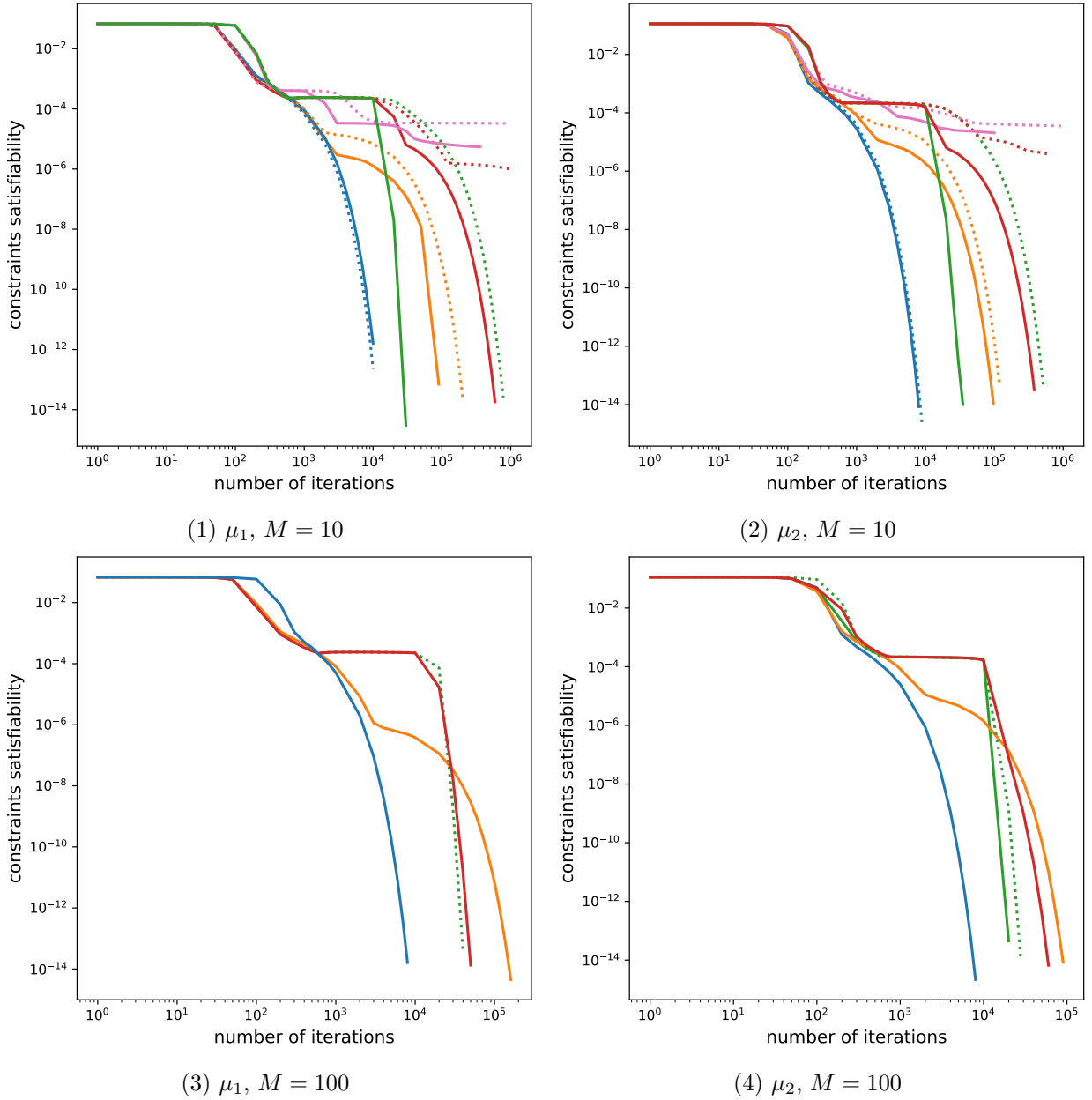


Figure 10: Evolution of $\|\Gamma^K(Y_m^K)\|_\infty$ for values of N ranging from 27 to 52 and K between 1000 (dotted lines) and 10000 (solid lines) as a function of the number of iterations m of the Runge-Kutta 3 procedure. $\Delta t_0 = 10^{-4}$. Blue curves are for $N = 27$, orange ones for $N = 37$, green ones for $N = 43$, red ones for $N = 52$ and pink ones for $N = 73$.

particle share the same weight, increasing the number of marginal laws relaxes the problem of finding a starting point on the submanifold.

5.2.3 Optimization procedure – Figures 11, 12, 13 and 14

The aim of Figures 11 and 12 is to plot the evolution of $V^K(Y_n^K)$ as a function of n the number of iterations of the constrained overdamped Langevin algorithm presented in Section 4 for various values of N and values of β_0 . As we observed (Figure 11), and similarly to the tests in dimension 1, that tests with $\beta_0 = 0$ converges faster than $\beta_0 > 0$, we kept $\beta_0 = 0$ for all the other tests. The convergence of the cost for various values of N and K , various number of marginal laws and for μ_1 and μ_2 is presented in Figure 12. And a presentation of how particles move during the optimization procedure

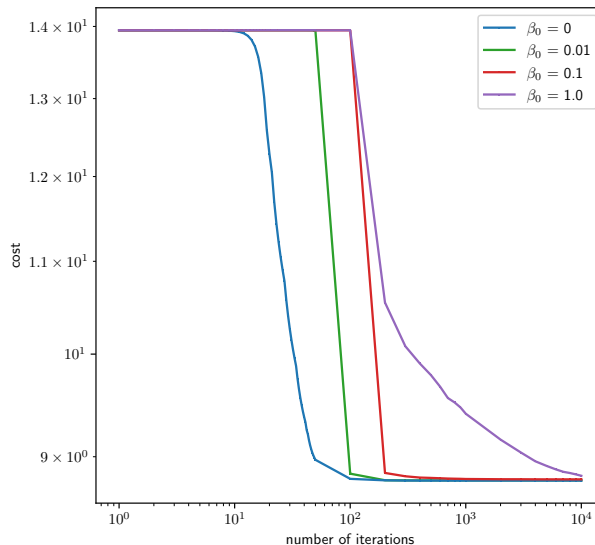


Figure 11: Evolution of the cost as a function of the number of iterations n for various values of β_0 . The marginal law is μ_2 , β_0 varies from 0 to 1 and the other parameters are $\Delta t_0 = 10^{-4}$, noise level decreases as the squareroot of the number of iterations, $N = 27$, $M = 10$, $K = 160$.

can be seen in Figures 13 and 14.

On all subgraphs of Figure 12, one can observe that the optimization procedure reaches a cost close to the optimal one for the MCOT problem in 50-200 iterations, when K is large enough for a given N (e.g. $K = 1000$ is sufficient when $N = 27$ but not when $N = 43$). As N increases the value of the optimal costs does as well, which is expected, as MCOT problems get more and more constrained. As K increases, the value of the cost computed converges towards the MCOT cost. Indeed, the slight decrease of the computed MCOT cost at the 20000th iteration as K increases that can be observed in Table 3 from $K = 320$ to $K = 10000$ suggests that there exists $K_0 \in \mathbb{N}$ such that for $K \geq K_0$, the gain in an increase in K reflects weakly on the MCOT cost computed.

On Figures 13 and 14 is plotted the evolution of some symmetrized visualizations of the process during the optimization for an MCOT problem on μ_1 . Although at each iteration it satisfies the moment constraints, it deviates from a Normal sample rapidly and tends to concentrate on some points (a bit like in Tchakaloff's theorem and [1, Theorem 3.1]).

5.2.4 Minimas – Figures 15, 16, 17 and 18

As K increases, the symmetrized minimizers of Figures 15 and 16 tends to be visually more and more concentrated on some particular points. According to Table 3, higher values of K tends to have lower costs.

Some symmetrized visualizations of minimizers for MCOT problems for the non-symmetrical measures μ_2 and μ_3 are presented in Figures 17 and 18. In those cases, the 1D couplings obtained on each axis (X, Y or Z) are not the same (Figure 17). A higher number of marginal laws M seems to spread more the particles, although their 1D coupling still shows particles highly concentrated around a few values in the considered examples. Higher values of N increases the concentration of the particles around fewer values in the μ_3 examples. The planar representation of the minimizers for large M (Figure 18), shows that particles are not distributed spatially as a Normal function and tend to concentrate on some 1D curves (for the considered 2D projections) with a higher spreading than for lower values of M .

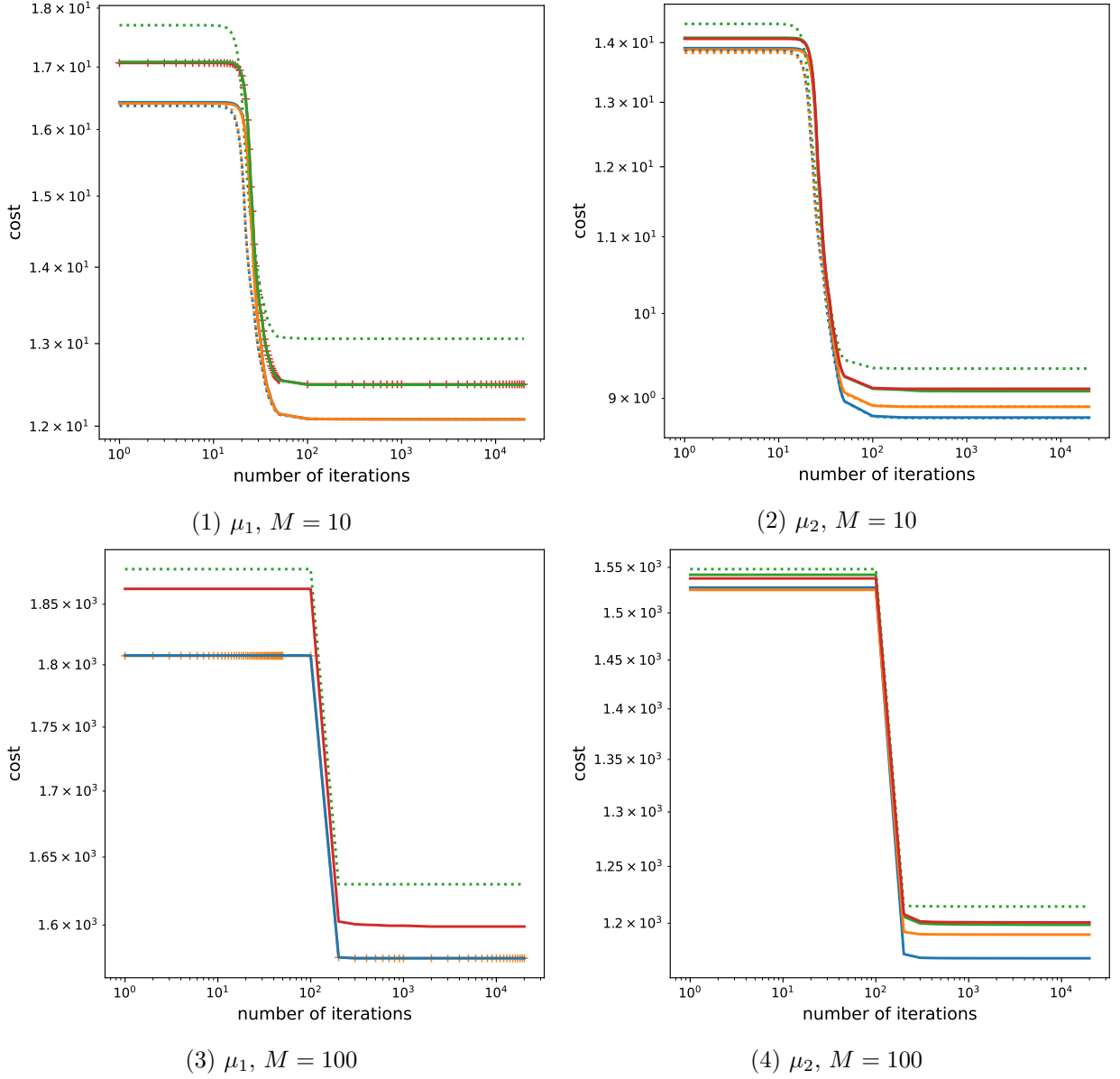
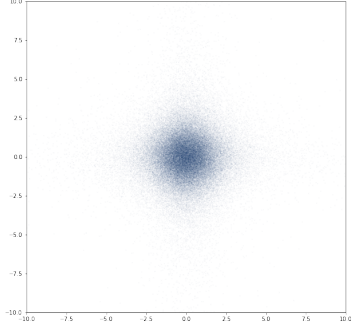


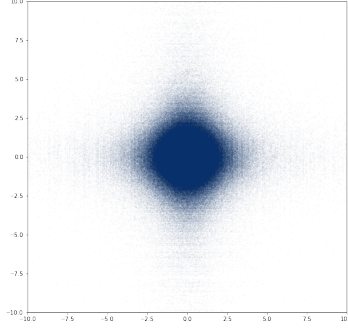
Figure 12: Evolution of the cost as a function of the number of iterations n for various values of N and K from 1000 (dotted lines) to 10000 (solid lines). $\Delta t_0 = 10^{-4}$, $\beta_0 = 0$. Blue curves are for $N = 27$, orange ones for $N = 37$, green ones for $N = 43$, red ones for $N = 52$ and pink ones for $N = 73$. On Figures 12.1 and 12.3, “+” signs are added to better distinguish overlaid curves.

K	40	80	160	320	1000	10000
cost	12.2558198	12.1747815	12.1457150	12.0916662	12.0821615	12.0785749
lower cost	12.1981977	12.0864398	12.0862042	12.0855486	12.0821615	12.0785745

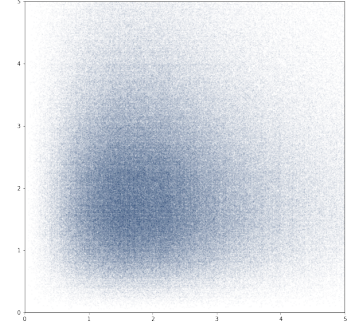
Table 3: Values of the regularized Coulomb cost (see here-named paragraph in Section 5.2.1) for the MCOT problem with μ_1 , $M = 10$, $N = 27$, $\Delta t_0 = 10^{-4}$, $\beta_0 = 0$ and K ranging from 40 to 10000. The *cost* line corresponds to the value of the regularized cost associated to the minimizing process at iteration 20000 (which also corresponds to the minimizers represented in the graphs of Figures 15 and 16). The *lower cost* line corresponds to the lower value of the regularized cost encountered by the minimizing process before or at iteration 20000 for each value of K .



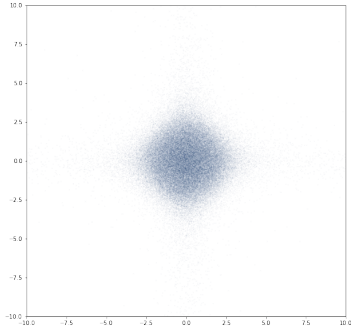
(a1) plane XY, iteration 1



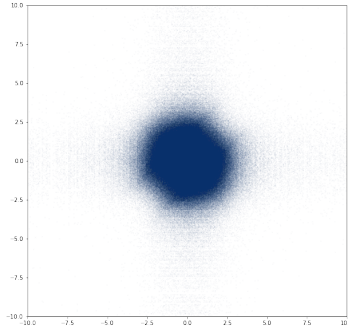
(b1) X axis, iteration 1



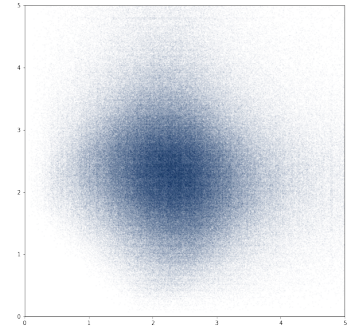
(c1) radial, iteration 1



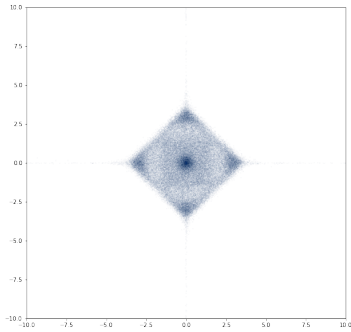
(a2) plane XY, iteration 30



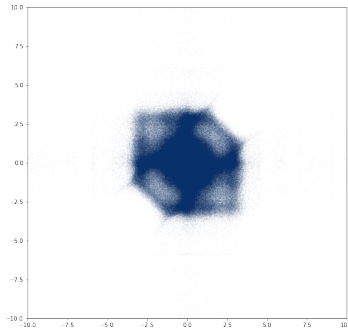
(b2) X axis, iteration 30



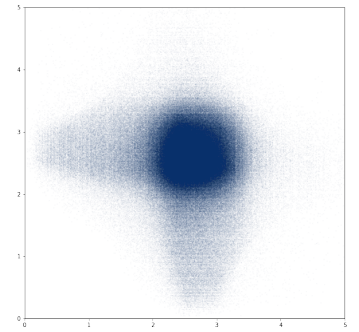
(c2) radial, iteration 30



(a3) plane XY, iteration 50

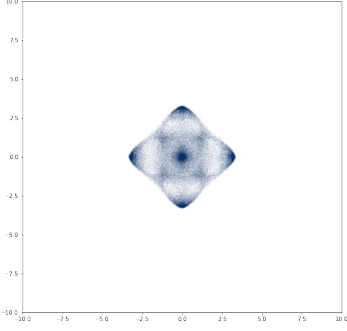


(b3) X axis, iteration 50

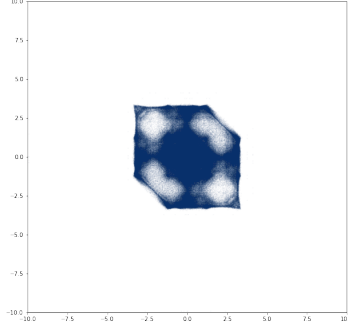


(c3) radial, iteration 50

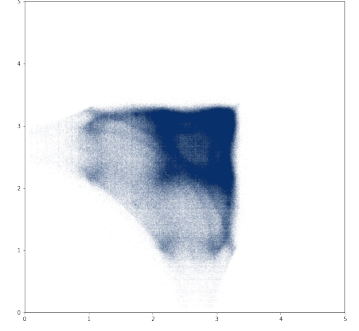
Figure 13: Transport along optimization for μ_1 , $M = 10$, $K = 10000$, $N = 27$, $\beta_0 = 0$, $\Delta t_0 = 10^{-4}$. In figures of column (a) is showed $\frac{1}{MK} \sum_{k=1}^K \sum_{m=1}^M \delta_{x_{m,1}^k, x_{m,2}^k}$. In figures of column (b) is showed $\frac{1}{M(M-1)K} \sum_{k=1}^K \sum_{m \neq m'=1}^M \delta_{x_{m,1}^k, x_{m',1}^k}$. In figures of column (c) is showed $\frac{1}{M(M-1)K} \sum_{k=1}^K \sum_{m \neq m'=1}^M \delta_{|x_m^k|, |x_{m'}^k|}$, where $|x_m^k| = \sqrt{\sum_{i=1}^3 (x_{m,i}^k)^2}$. The evolution of the corresponding cost can be seen in Figure 12.1.



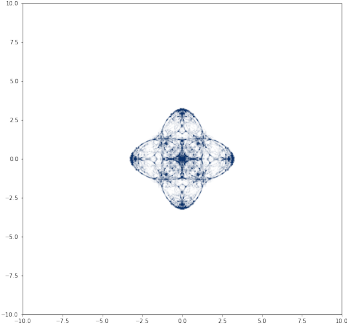
(a4) plane XY, iteration 100



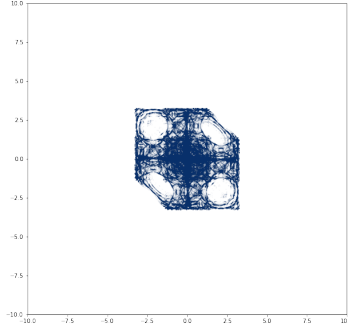
(b4) X axis, iteration 100



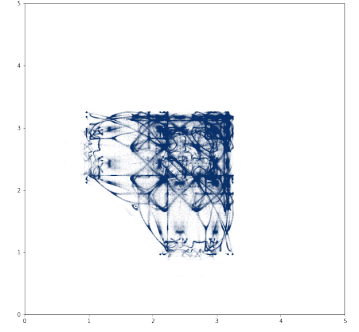
(c4) radial, iteration 100



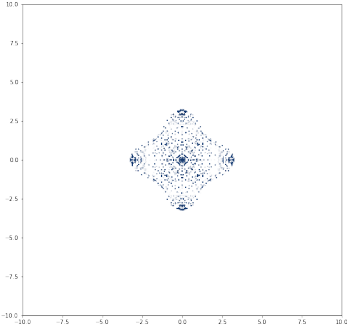
(a5) plane XY, iteration 1000



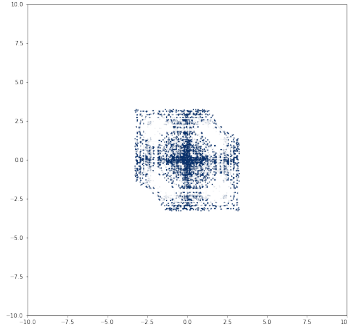
(b5) X axis, iteration 1000



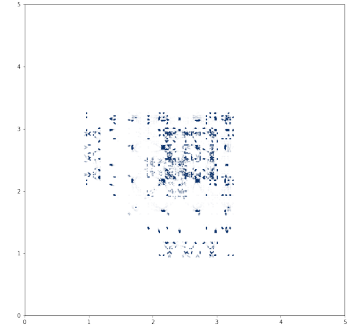
(c5) radial, iteration 1000



(a6) plane XY, iteration 20000



(b6) X axis, iteration 20000



(c6) radial, iteration 20000

Figure 14: Transport along optimization for μ_1 , $M = 10$, $K = 10000$, $N = 27$, $\beta_0 = 0$, $\Delta t_0 = 10^{-4}$. In figures of column (a) is showed $\frac{1}{MK} \sum_{k=1}^K \sum_{m=1}^M \delta_{x_{m,1}^k, x_{m,2}^k}$. In figures of column (b) is showed $\frac{1}{M(M-1)K} \sum_{k=1}^K \sum_{m \neq m'=1}^M \delta_{x_{m,1}^k, x_{m',1}^k}$. In figures of column (c) is showed $\frac{1}{M(M-1)K} \sum_{k=1}^K \sum_{m \neq m'=1}^M \delta_{|x_m^k|, |x_{m'}^k|}$, where $|x_m^k| = \sqrt{\sum_{i=1}^3 (x_{m,i}^k)^2}$. The evolution of the corresponding cost can be seen in Figure 12.1.

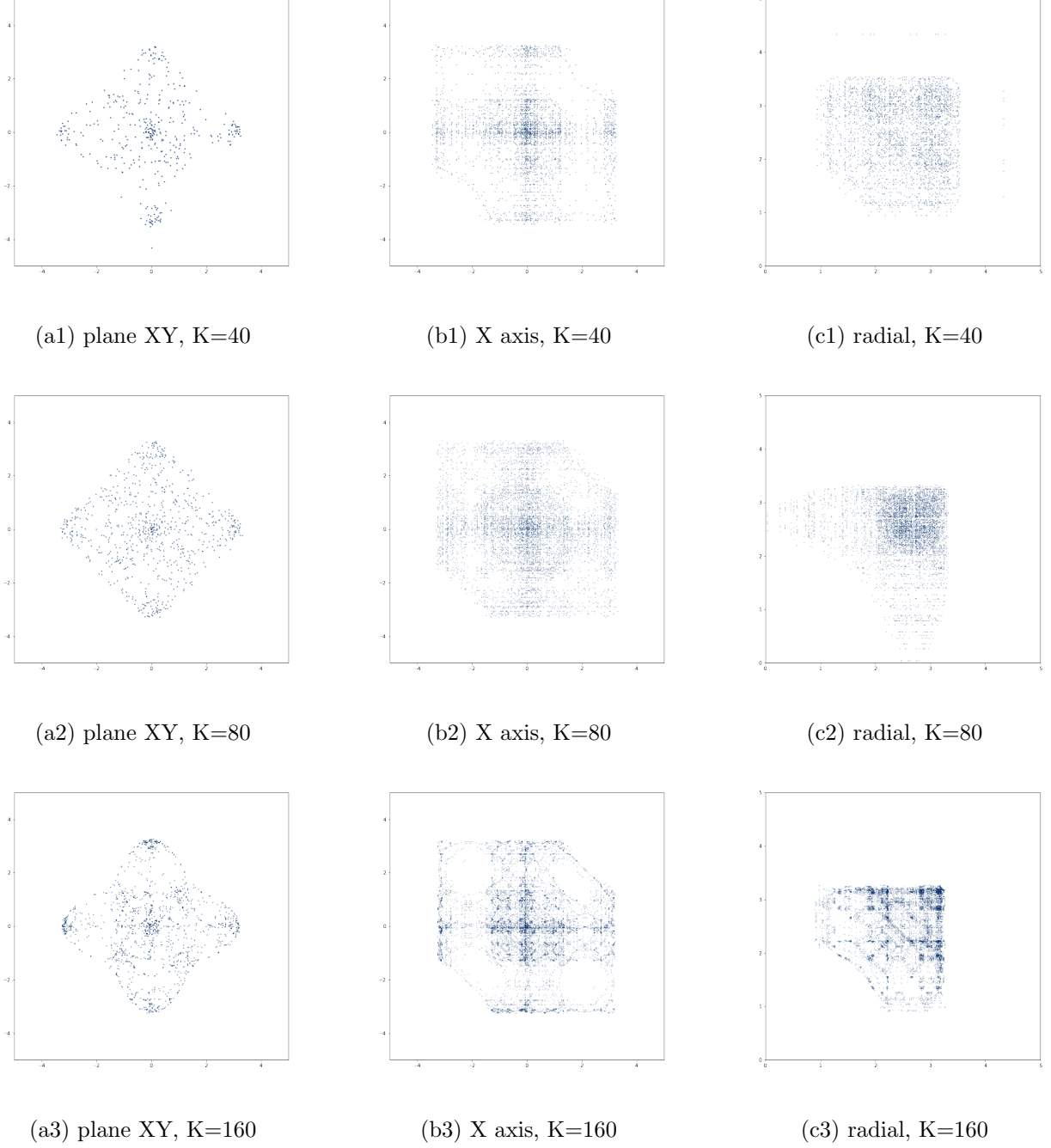


Figure 15: Optimal transport with μ_1 , $M = 10$, $N = 27$, $\beta_0 = 0$ and $\Delta t_0 = 10^{-4}$, for $K = 40, 80, 160$. In figures of column (a) is showed $\frac{1}{MK} \sum_{k=1}^K \sum_{m=1}^M \delta_{x_{m,1}^k, x_{m,2}^k}$. In figures of column (b) is showed $\frac{1}{M(M-1)K} \sum_{k=1}^K \sum_{m \neq m'=1}^M \delta_{x_{m,1}^k, x_{m',1}^k}$. In figures of column (c) is showed $\frac{1}{M(M-1)K} \sum_{k=1}^K \sum_{m \neq m'=1}^M \delta_{|x_m^k|, |x_{m'}^k|}$, where $|x_m^k| = \sqrt{\sum_{i=1}^3 (x_{m,i}^k)^2}$. Corresponding costs can be found in Table 3.

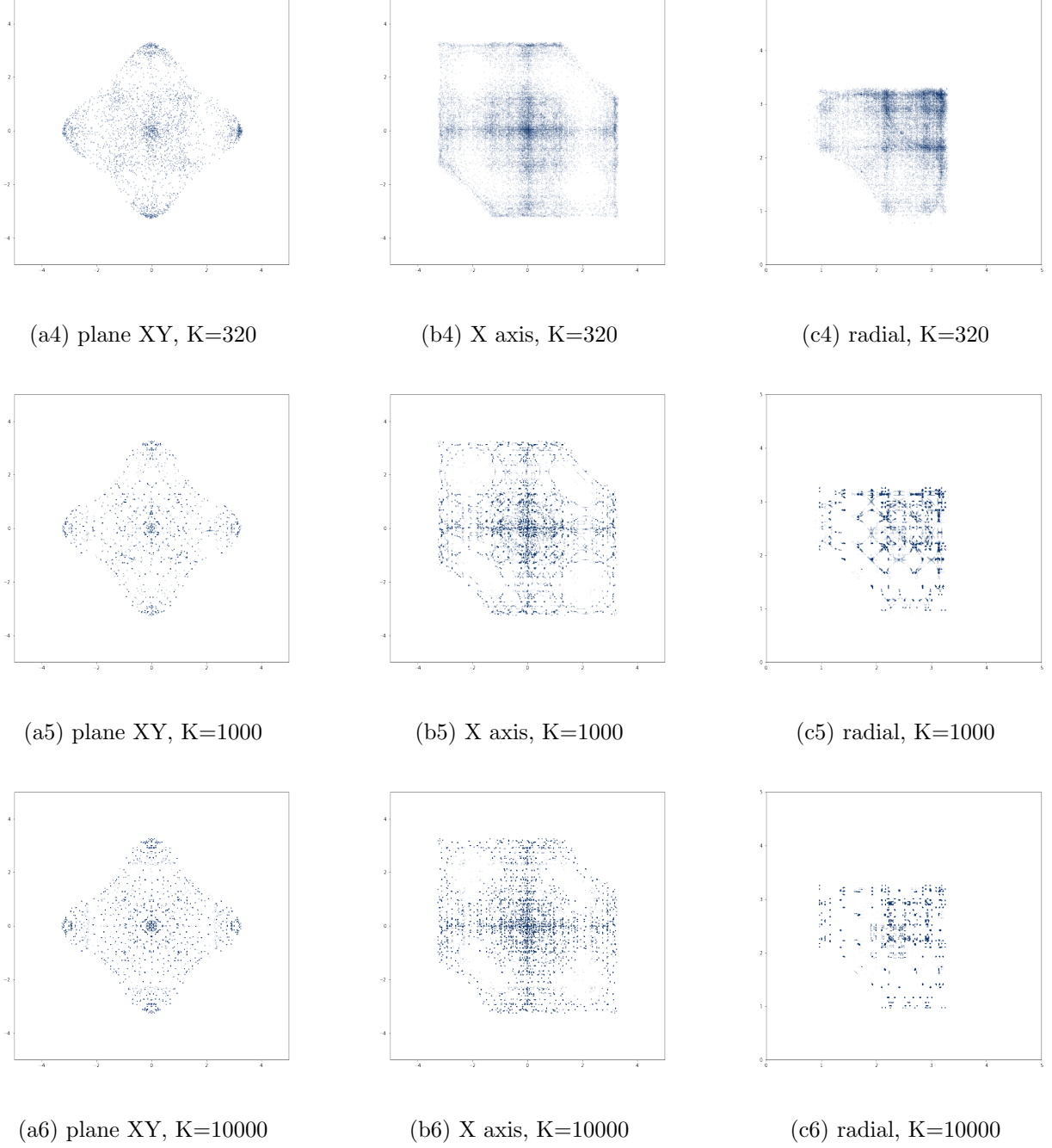


Figure 16: Optimal transport with μ_1 , $M = 10$, $N = 27$, $\beta_0 = 0$ and $\Delta t_0 = 10^{-4}$, for $K = 320, 1000, 10000$. In figures of column (a) is showed $\frac{1}{MK} \sum_{k=1}^K \sum_{m=1}^M \delta_{x_{m,1}^k, x_{m,2}^k}$. In figures of column (b) is showed $\frac{1}{M(M-1)K} \sum_{k=1}^K \sum_{m \neq m'=1}^M \delta_{x_{m,1}^k, x_{m',1}^k}$. In figures of column (c) is showed $\frac{1}{M(M-1)K} \sum_{k=1}^K \sum_{m \neq m'=1}^M \delta_{|x_m^k|, |x_{m'}^k|}$, where $|x_m^k| = \sqrt{\sum_{i=1}^3 (x_{m,i}^k)^2}$. Corresponding costs can be found in Table 3.

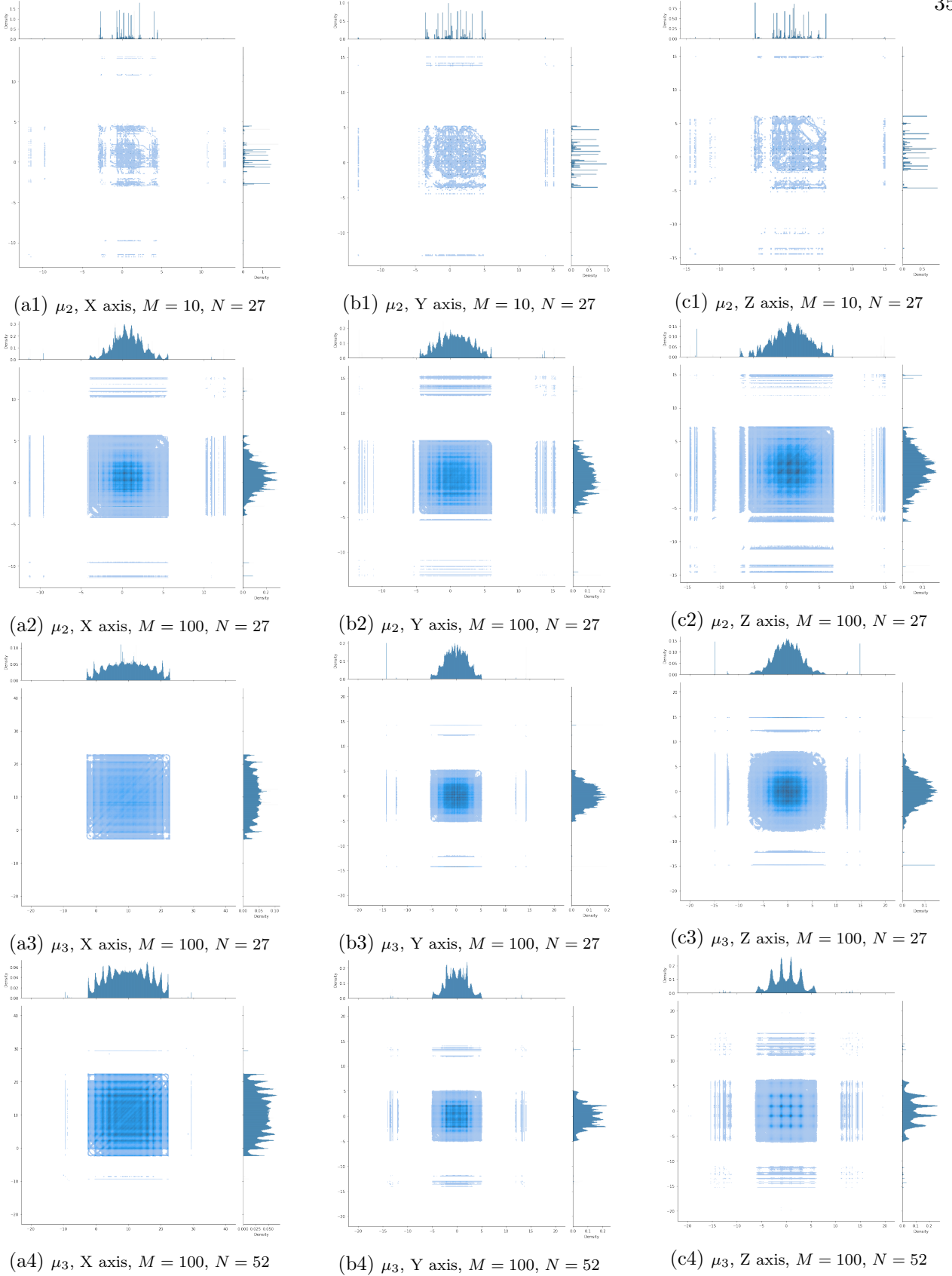


Figure 17: Optimal transport for μ_2 and μ_3 , $M = 10, 100$, $N = 27, 52$, $\beta_0 = 0$, $K = 10000$ and $\Delta t_0 = 10^{-4}$. In figures of column (a) is showed $\frac{1}{MK} \sum_{k=1}^K \sum_{m=1}^M \delta_{x_{m,1}^k, x_{m,2}^k}$. In figures of column (b) is showed $\frac{1}{M(M-1)K} \sum_{k=1}^K \sum_{m \neq m'=1}^M \delta_{x_{m,1}^k, x_{m',1}^k}$. In figures of column (c) is showed $\frac{1}{M(M-1)K} \sum_{k=1}^K \sum_{m \neq m'=1}^M \delta_{|x_m^k|, |x_{m'}^k|}$, where $|x_m^k| = \sqrt{\sum_{i=1}^3 (x_{m,i}^k)^2}$. In order to better distinguish between areas of low and high particles density, plots are represented as 2D histograms.

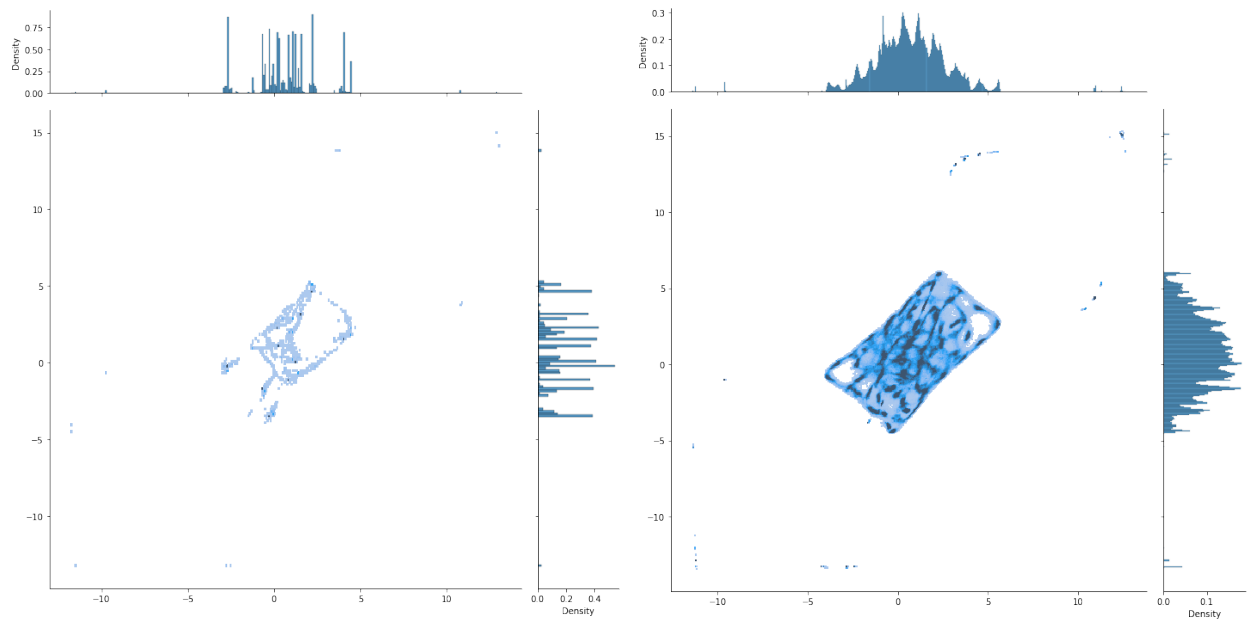
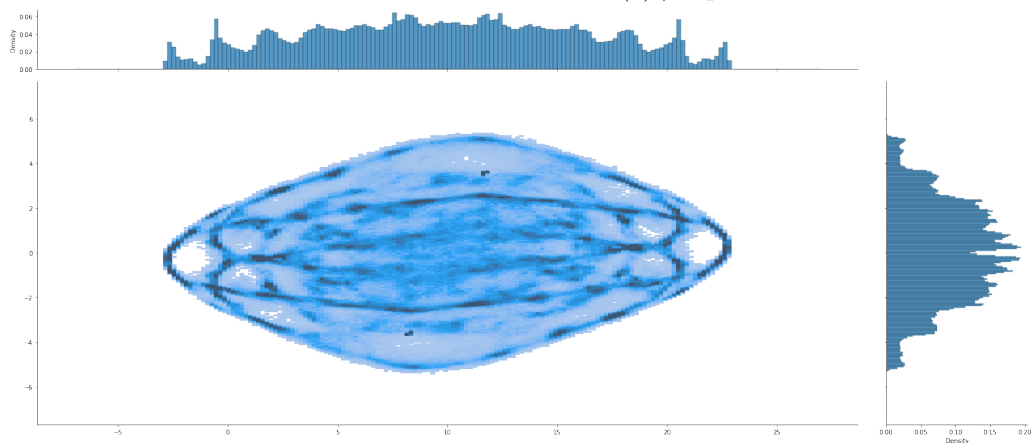
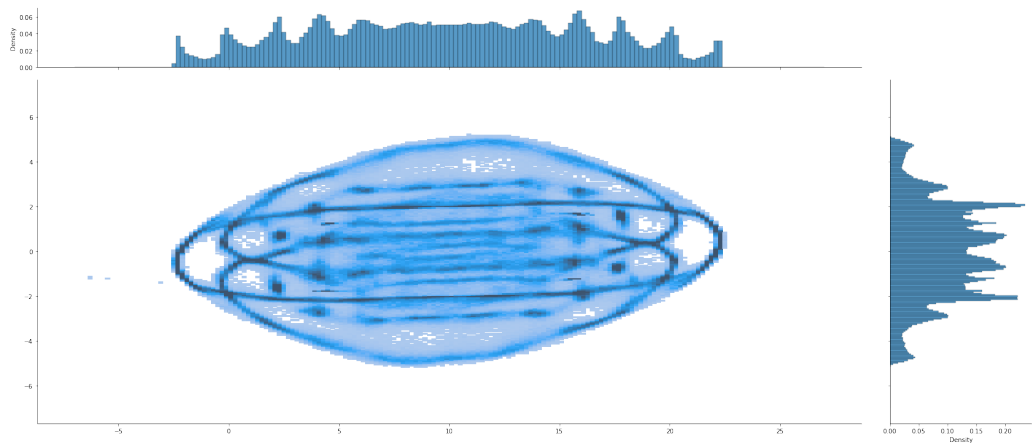
(1) μ_2 , plane XY, $M = 10$, $N = 27$ (2) μ_2 , plane XY, $M = 100$, $N = 27$ (3) μ_3 , plane XY, $M = 100$, $N = 27$ (4) μ_3 , plane XY, $M = 100$, $N = 52$

Figure 18: Optimal transport for μ_2 and μ_3 , $M = 10, 100$, $N = 27, 52$, $\beta_0 = 0$, $K = 10000$ and $\Delta t_0 = 10^{-4}$. In each graph, minimizers are represented as $\frac{1}{MK} \sum_{k=1}^K \sum_{m=1}^M \delta_{x_{m,1}^k, x_{m,2}^k}$. In order to better distinguish between areas of low and high particles density, plots are represented as 2D histograms.

5.2.5 Optimization for μ_4 - Figure 19

Optimal transport for μ_4 with a large number of electrons is of theoretical interest as it might provide approximations for a uniform electronic density in a large space [32]. Numerical results for its MCOT relaxation with $M = 100$ and $N = 52$ are presented in Figure 19. Although the cost has been optimized (Figure 19.1), it is only 3% lower than the initial uniform sampling (after a Runge-Kutta 3 initialization). Although the 1D marginal laws seem well approximated (Figures 19.2 and 19.3), planar and radial graphs (Figures 19.2 and 19.4) show that particles are concentrated on two spheres (of radius 0.6 and 1 respectively). Most of the transport takes place inside and between those two spheres.

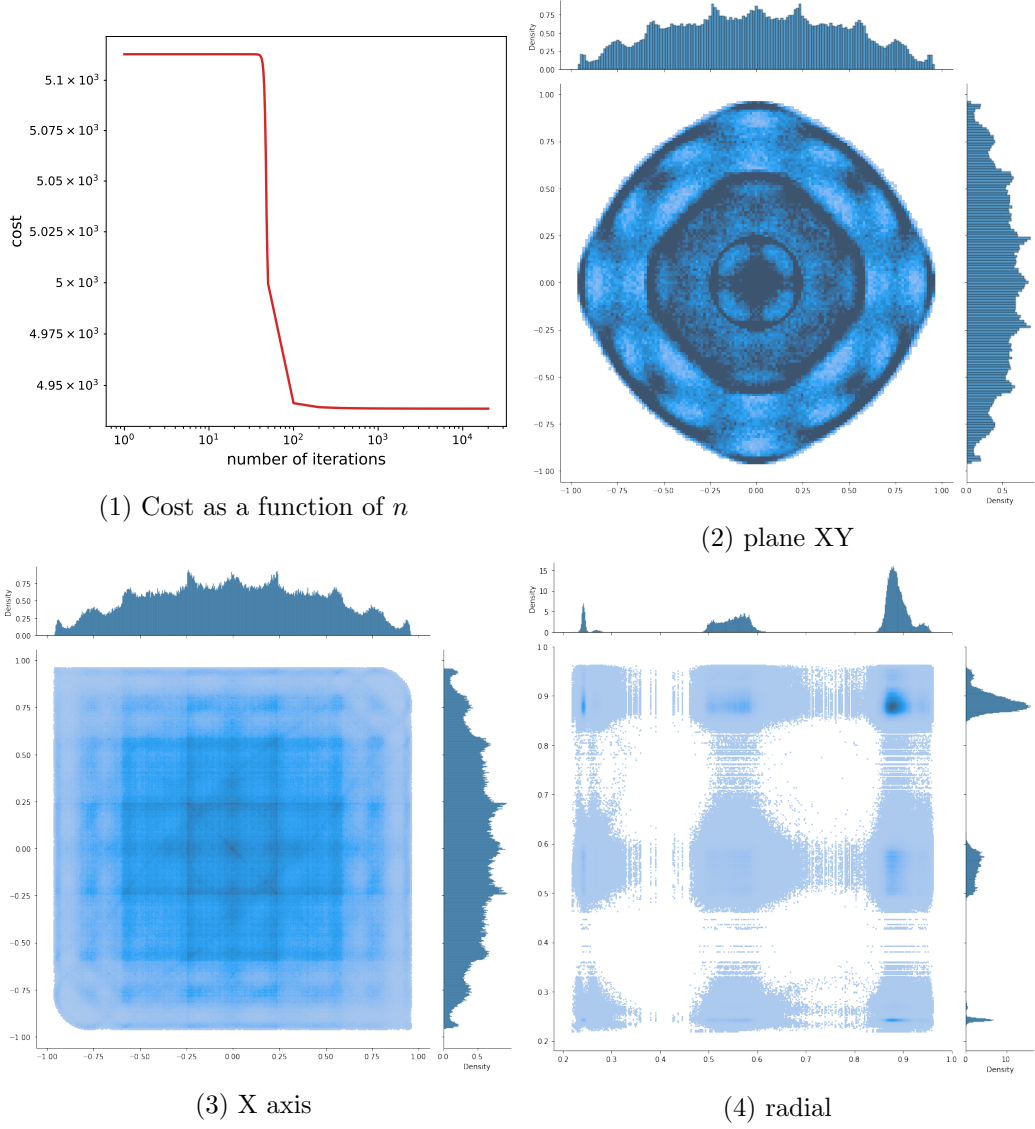


Figure 19: Evolution of the cost as a function of the number of iteration n (Figure 19.1) and optimal transport with μ_4 , $M = 100$, $N = 52$, $K = 10000$, $\beta_0 = 0$ and $\Delta t_0 = 10^{-4}$. In Figure 19.2 is showed $\frac{1}{MK} \sum_{k=1}^K \sum_{m=1}^M \delta_{x_{m,1}^k, x_{m,2}^k}$. In Figure 19.3 is showed $\frac{1}{M(M-1)K} \sum_{k=1}^K \sum_{m \neq m'=1}^M \delta_{x_{m,1}^k, x_{m',1}^k}$. In Figure 19.4 is showed $\frac{1}{M(M-1)K} \sum_{k=1}^K \sum_{m \neq m'=1}^M \delta_{|x_m^k|, |x_{m'}^k|}$, where $|x_m^k| = \sqrt{\sum_{i=1}^3 (x_{m,i}^k)^2}$. In order to better distinguish between areas of low and high particles density, plots are represented as 2D histograms.

6 Proof of Theorem 1

The aim of this section is to gather the proofs of our main theoretical results.

6.1 Tchakaloff's theorem

We present here a corollary of the so-called Tchakaloff theorem which is the backbone of our results concerning the theoretical properties of the MCOT particle problem. A general version of the Tchakaloff theorem has been proved by Bayer and Teichmann [2]. Theorem 4 is an immediate consequence of Tchakaloff's theorem, see Corollary 2 in [2].

Theorem 4. *Let π be a measure on \mathbb{R}^d concentrated on a Borel set $A \in \mathcal{F}$, i.e. $\pi(\mathbb{R}^d \setminus A) = 0$. Let $N_0 \in \mathbb{N}^*$ and $\Lambda : \mathbb{R}^d \rightarrow \mathbb{R}^{N_0}$ a measurable Borel map. Assume that the first moments of $\Lambda\#\pi$ exist, i.e.*

$$\int_{\mathbb{R}^{N_0}} \|u\| d\Lambda\#\pi(u) = \int_{\mathbb{R}^d} \|\Lambda(z)\| d\pi(z) < \infty,$$

where $\|\cdot\|$ denotes the Euclidean norm of \mathbb{R}^{N_0} . Then, there exist an integer $1 \leq K \leq N_0$, points $z_1, \dots, z_K \in A$ and weights $p_1, \dots, p_K > 0$ such that

$$\forall 1 \leq i \leq N_0, \quad \int_{\mathbb{R}^d} \Lambda_i(z) d\pi(z) = \sum_{k=1}^K p_k \Lambda_i(z_k),$$

where Λ_i denotes the i -th component of Λ .

We recall here that $\Lambda\#\pi$ is the push-forward of π through Λ , and is defined as $\Lambda\#\pi(A) = \pi(\Lambda^{-1}(A))$ for any Borel set $A \subset \mathbb{R}^{N_0}$.

Last, let us mention that Theorem 4 is a consequence of Caratheodory's theorem [42, Corollary 17.1.2] applied to $\int_{\mathbb{R}^{N_0}} u d\Lambda\#\pi(u)$ which lies in the (convex) cone induced by $\text{spt}(\Lambda\#\pi)$, the support of the measure $\Lambda\#\pi$.

6.2 Proof of Theorem 1

We denote here by \mathcal{S}_K the set of permutations of the set $\{1, \dots, K\}$.

Lemma 5. *Let $(W, Y) \in \mathcal{U}_K^N$ be such that there exists k' such that $w_{k'} = 0$. Then for any permutation $\sigma \in \mathcal{S}_K$, there exists a polygonal map $\psi : [0, 1] \rightarrow \mathcal{U}_K^N$ such that $\psi(0) = (W, Y)$, $\psi(1) = (W^\sigma, Y^\sigma)$ and $\mathcal{I}(\psi(t))$ is constant, where $Y^\sigma := (X^{\sigma(k)})_{1 \leq k \leq K} \in ((\mathbb{R}^d)^M)^K$ and $W^\sigma := (w_{\sigma(k)})_{1 \leq k \leq K} \in (\mathbb{R}_+)^K$.*

Proof. For (W, Y) and (W', Y') , we will denote $[(W, Y), (W', Y')]$ the segment map $t \in [0, 1] \mapsto [(1-t)W + tW', (1-t)Y + tY']$ and we will construct ψ as the concatenation of segments that are clearly in \mathcal{U}_K^N and leaves \mathcal{I} constant.

It is sufficient to prove this result for transpositions i.e. for σ such that there exist $i_1 < i_2$ such that $\sigma(i_1) = i_2$, $\sigma(i_2) = i_1$ and $\sigma(i) = i$ for $i \notin \{i_1, i_2\}$. We distinguish two cases.

- $k' \in \{i_1, i_2\}$, say $k' = i_2$. We then define $Y_1 = (X_1^k)_{1 \leq k \leq K}$ by $X_1^{k'} = X^{i_1}$ and $X_1^k = X^k$ for $k \neq k'$ and consider the segment $[(W, Y), (W, Y_1)]$. We then set $w_1^{k'} = w^{i_1}$, $w_1^{i_1} = 0$ and $w_1^k = w^k$ for $k \notin \{k', i_1\}$ (note that $W_1 = W^\sigma$) and consider the segment $[(W, Y_1), (W_1, Y_1)]$. Last, we define $Y_2 = (X_2^k)_{1 \leq k \leq K}$ as $X_2^{i_1} = X^{k'}$ and $X_2^k = X_1^k$ for $k \neq i_1$ (note that $Y_2 = Y^\sigma$) and consider the segment $[(W_1, Y_1), (W_1, Y_2)]$.
- $k' \notin \{i_1, i_2\}$. First, we define $Y_1 = (X_1^k)_{1 \leq k \leq K}$ by $X_1^{k'} = X^{i_1}$ and $X_1^k = X^k$ for $k \neq k'$ and consider the segment $[(W, Y), (W, Y_1)]$. We then set $w_1^{k'} = w^{i_1}$, $w_1^{i_1} = 0$ and $w_1^k = w^k$ for $k \notin \{k', i_1\}$ and consider the segment $[(W, Y_1), (W_1, Y_1)]$. Then, we define $Y_2 = (X_2^k)_{1 \leq k \leq K}$ as $X_2^{i_1} = X^{i_2}$ and $X_2^k = X_1^k$ for $k \neq i_1$, and consider the segment $[(W_1, Y_1), (W_1, Y_2)]$. We the set $w_2^{i_1} = w^{i_2}$, $w_2^{i_2} = 0$ and $w_2^k = w_1^k$ for $k \notin \{i_1, i_2\}$, and consider the segment $[(W_1, Y_2), (W_2, Y_2)]$.

Now, we define $Y_3 = (X_3^k)_{1 \leq k \leq K}$ by $X_3^{i_2} = X^{i_1}$, $X_3^k = X_2^k$ for $k \neq i_2$ and consider the segment $[(W_2, Y_2), (W_2, Y_3)]$. Then, we define $w_3^{i_2} = w_2^{k'} = w^{i_1}$, $w_3^{k'} = 0$ and $w_3^k = w_2^k$ for $k \notin \{i_2, k'\}$ (note that $W_3 = W^\sigma$) and consider the segment $[(W_2, Y_3), (W_3, Y_3)]$. Last, we set $Y_4 = (X_4^k)_{1 \leq k \leq K}$ with $X_4^{k'} = X^{k'}$ and $X_4^k = X_3^k$ for $k \neq k'$ (note that $Y_4 = Y^\sigma$) and finally consider the segment $[(W_3, Y_3), (W_3, Y_4)]$, which gives the claim. \square

Proof. For $i = 0, 1$, let $W_i := (w_{k,i})_{1 \leq k \leq K} \in \mathbb{R}_+^K$, $Y_i = (X_i^k)_{1 \leq k \leq K} \subset (\mathbb{R}^d)^M$ and $\pi_i := \sum_{k=1}^K w_{k,i} \delta_{X_i^k} \in \mathcal{P}((\mathbb{R}^d)^M)$. Note that, for $i = 0, 1$, the support of π_i is included in the discrete set $\{X_i^k, 1 \leq k \leq K\}$.

For $i = 0, 1$, using Theorem 4 with $\pi = \pi_i$ and $\Lambda : (\mathbb{R}^d)^M \rightarrow \mathbb{R}^{N+3}$ the map defined such that, for all $X \in (\mathbb{R}^d)^M$,

$$\Lambda_n(X) = \varphi_n(X), \quad \forall 1 \leq n \leq N, \quad \Lambda_{N+1}(X) = 1, \quad \Lambda_{N+2}(X) = c(X) \quad \text{and} \quad \Lambda_{N+3}(X) = \vartheta(X),$$

it holds that there exists a subset $J^i \subset \{1, \dots, K\}$ such that $K_i := \#J^i \leq N + 3$, and weights $(\tilde{w}_j^i)_{j \in J^i} \subset \mathbb{R}_+$ such that

$$\forall 1 \leq n \leq N, \quad \sum_{j \in J^i} \tilde{w}_j^i \varphi_n(X_j^j) = \int_{(\mathbb{R}^d)^M} \varphi_n d\pi_i = \sum_{k=1}^K w_{k,i} \varphi_n(X_i^k) = \mu_n, \quad (48)$$

$$\sum_{j \in J^i} \tilde{w}_j^i = \int_{(\mathbb{R}^d)^M} d\pi_i = \sum_{k=1}^K w_{k,i} = 1, \quad (49)$$

$$\sum_{j \in J^i} \tilde{w}_j^i c(X_j^j) = \int_{(\mathbb{R}^d)^M} c d\pi_i = \sum_{k=1}^K w_{k,i} c(X_i^k) = \mathcal{I}(W_i, Y_i), \quad (50)$$

$$\sum_{j \in J^i} \tilde{w}_j^i \vartheta(X_j^j) = \int_{(\mathbb{R}^d)^M} \vartheta d\pi_i = \sum_{k=1}^K w_{k,i} \vartheta(X_i^k) \leq A. \quad (51)$$

Without loss of generality, by using Lemma 5, we can assume that $J^0 = \llbracket 1, K_0 \rrbracket$ where $K_0 \leq N + 3$ and that $J^1 = \llbracket K - K_1 + 1, K \rrbracket$ where $K - K_1 + 1 \geq N + 4$.

We then define $\widetilde{W}_0 := (\tilde{w}_1^0, \dots, \tilde{w}_{K_0}^0, 0, \dots, 0) \in \mathbb{R}_+^K$ and $\widetilde{W}_1 := (0, \dots, 0, \tilde{w}_{K-K_1+1}^1, \dots, \tilde{w}_K^1) \in \mathbb{R}_+^K$. Let us first define the applications

$$\psi_1 : \left[0, \frac{1}{5}\right] \ni t \mapsto (W_0 + 5t(\widetilde{W}_0 - W_0), Y_0)$$

and

$$\psi_5 : \left[\frac{4}{5}, 1\right] \ni t \mapsto (W_1 + 5(1-t)(\widetilde{W}_1 - W_1), Y_1)$$

so that $\psi_0(0) = (W_0, Y_0)$, $\psi_0(1/5) = (\widetilde{W}_0, Y_0)$, $\psi_1(1) = (W_1, Y_1)$, $\psi_1(4/5) = (\widetilde{W}_1, Y_1)$. Then, ψ_0 and ψ_1 are continuous applications and identities (48)-(49)-(50)-(51) implies that for all $t \in [0, 1/5]$ (respectively all $t \in [4/5, 1]$), $\psi_0(t) \in \mathcal{U}_N^K$ and $\mathcal{I}(\psi_0(t)) = \mathcal{I}(W_0, Y_0)$ (respectively $\psi_1(t) \in \mathcal{U}_N^K$ and $\mathcal{I}(\psi_1(t)) = \mathcal{I}(W_1, Y_1)$).

We then define $\widetilde{Y} := (X_0^1, \dots, X_0^{K_0}, 0, \dots, 0, X_1^{K-K_1+1}, \dots, X_1^K) \in ((\mathbb{R}^d)^M)^K$. We then introduce the continuous applications

$$\psi_2 : \left[\frac{1}{5}, \frac{2}{5}\right] \ni t \mapsto (\widetilde{W}_0, Y_0 + 5(t - 1/5)\widetilde{Y})$$

and

$$\psi_4 : \left[\frac{3}{5}, \frac{4}{5} \right] \ni t \mapsto \left(\widetilde{W}_1, Y_1 + 5(4/5 - t)\widetilde{Y} \right).$$

It thus holds that $\psi_2(1/5) = (\widetilde{W}_0, Y_0)$ and $\psi_2(2/5) = (\widetilde{W}_0, \widetilde{Y})$. Similarly, $\psi_4(4/5) = (\widetilde{W}_1, Y_1)$ and $\psi_4(3/5) = (\widetilde{W}_1, \widetilde{Y})$. Let us point out here that, by the definition of \widetilde{Y} , for any $t \in [\frac{1}{5}, \frac{2}{5}]$, the K_0 first components of $\psi_2(t)$ are equal to $X_0^1, \dots, X_0^{K_0}$. Thus, since $\widetilde{W}_0 := (\widetilde{w}_1^0, \dots, \widetilde{w}_{K_0}^0, 0, \dots, 0) \in \mathbb{R}_+^K$, this implies that for all $t \in [\frac{1}{5}, \frac{2}{5}]$, $\psi_2(t) \in \mathcal{U}_N^K$ and in addition,

$$\mathcal{I}(\psi_2(t)) = \mathcal{I}(\widetilde{W}_0, Y_0) = \mathcal{I}(\widetilde{W}_0, \widetilde{Y}) = \mathcal{I}(W_0, Y_0).$$

Similarly, for any $t \in [\frac{3}{5}, \frac{4}{5}]$, $\psi_4(t) \in \mathcal{U}_N^K$ and in addition,

$$\mathcal{I}(\psi_4(t)) = \mathcal{I}(\widetilde{W}_1, Y_1) = \mathcal{I}(\widetilde{W}_1, \widetilde{Y}) = \mathcal{I}(W_1, Y_1).$$

Notice that in particular, \mathcal{I} remains constant along the paths in \mathcal{U}_N^K given by the applications ψ_1 , ψ_2 , ψ_4 and ψ_5 .

Last, we introduce the application

$$\psi_3 : \left[\frac{2}{5}, \frac{3}{5} \right] \ni t \mapsto \left(\widetilde{W}_0 + 5(t - 2/5)\widetilde{W}_1, \widetilde{Y} \right)$$

which is continuous and such that $\psi_3(2/5) = (\widetilde{W}_0, \widetilde{Y})$ and $\psi_3(3/5) = (\widetilde{W}_1, \widetilde{Y})$. Using similar arguments as above, it then holds that for all $t \in [2/5, 3/5]$, $\psi_3(t) \in \mathcal{P}_N^K$ and

$$\mathcal{I}(\psi_3(t)) = \mathcal{I}(\widetilde{W}_0, \widetilde{Y}) + 5(t - 2/5)\mathcal{I}(\widetilde{W}_1, \widetilde{Y}) = \mathcal{I}(W_0, Y_0) + 5(t - 2/5)\mathcal{I}(W_1, Y_1).$$

This implies that \mathcal{I} monotonically varies along the path given by the application ψ_3 .

We finally consider the application $\psi : [0, 1] \rightarrow (\mathbb{R}_+)^K \times ((\mathbb{R}^d)^M)^K$ defined by

$$\forall t \in [0, 1], \quad \psi(t) = \begin{cases} \psi_1(t) & \text{if } t \in [0, 1/5], \\ \psi_2(t) & \text{if } t \in [1/5, 2/5], \\ \psi_3(t) & \text{if } t \in [2/5, 3/5], \\ \psi_4(t) & \text{if } t \in [3/5, 4/5], \\ \psi_5(t) & \text{if } t \in [4/5, 1]. \end{cases}$$

Gathering all the results we have obtained so far, it then holds that ψ is continuous, that for all $t \in [0, 1]$, $\psi(t) \in \mathcal{U}_N^K$ and that the application $\mathcal{I} \circ \psi$ is monotone. Hence the desired result. \square

Acknowledgements

The Labex Bézout is acknowledged for funding the PhD thesis of Rafaël Coyaud. Aurélien Alfonsi benefited from the support of the ‘‘Chaire Risques Financiers’’, Fondation du Risque. We are very grateful to Gero Friesecke, Daniela Vögler, Tony Lelièvre, Gabriel Stoltz and Pierre Monmarché for stimulating discussions, as well as Mathieu Lewin for precious comments on the paper. This publication is part of a project that has received funding from the European Research Council (ERC) under the European Union’s Horizon 2020 Research and Innovation Programme – Grant Agreement n° 810367.

References

- [1] Aurélien Alfonsi, Rafaël Coyaud, Virginie Ehrlacher, and Damiano Lombardi. Approximation of optimal transport problems with marginal moments constraints. *Math. Comp.*, 90(328):689–737, 2021.
- [2] Christian Bayer and Josef Teichmann. The proof of Tchakaloff’s theorem. *Proceedings of the American mathematical society*, 134(10):3035–3040, 2006.
- [3] Mathias Beiglböck, Pierre Henry-Labordère, and Friedrich Penkner. Model-independent bounds for option prices—a mass transport approach. *Finance Stoch.*, 17(3):477–501, 2013.
- [4] Jean-David Benamou, Guillaume Carlier, Marco Cuturi, Luca Nenna, and Gabriel Peyré. Iterative bregman projections for regularized transportation problems. *SIAM Journal on Scientific Computing*, 37(2):A1111–A1138, 2015.
- [5] Jean-David Benamou, Guillaume Carlier, and Luca Nenna. A numerical method to solve multi-marginal optimal transport problems with coulomb cost. In *Splitting Methods in Communication, Imaging, Science, and Engineering*, pages 577–601. Springer, 2016.
- [6] Ugo Bindini and Luigi De Pascale. Optimal transport with Coulomb cost and the semiclassical limit of density functional theory. *J. Éc. polytech. Math.*, 4:909–934, 2017.
- [7] Giuseppe Buttazzo, Thierry Champion, and Luigi De Pascale. Continuity and estimates for multimarginal optimal transportation problems with singular costs. *Appl. Math. Optim.*, 78(1):185–200, 2018.
- [8] Giuseppe Buttazzo, Luigi De Pascale, and Paola Gori-Giorgi. Optimal-transport formulation of electronic density-functional theory. *Physical Review A*, 85(6):062502, 2012.
- [9] Guillaume Carlier. Optimal transportation and economic applications. *Lecture Notes*, 2012.
- [10] Guillaume Carlier, Vincent Duval, Gabriel Peyré, and Bernhard Schmitzer. Convergence of entropic schemes for optimal transport and gradient flows. *SIAM J. Math. Anal.*, 49(2):1385–1418, 2017.
- [11] Giovanni Ciccotti, Tony Lelièvre, and Eric Vanden-Eijnden. Projection of diffusions on submanifolds: Application to mean force computation. *Communications on Pure and Applied Mathematics: A Journal Issued by the Courant Institute of Mathematical Sciences*, 61(3):371–408, 2008.
- [12] Maria Colombo, Luigi De Pascale, and Simone Di Marino. Multimarginal optimal transport maps for one-dimensional repulsive costs. *Canadian Journal of Mathematics*, 67(2):350–368, 2015.
- [13] Codina Cotar, Gero Friesecke, and Claudia Klüppelberg. Density functional theory and optimal transportation with coulomb cost. *Communications on Pure and Applied Mathematics*, 66(4):548–599, 2013.
- [14] Codina Cotar, Gero Friesecke, and Claudia Klüppelberg. Smoothing of transport plans with fixed marginals and rigorous semiclassical limit of the hohenberg–kohn functional. *Archive for Rational Mechanics and Analysis*, 228(3):891–922, 2018.
- [15] Dinh Dũng, Vladimir Temlyakov, and Tino Ullrich. *Hyperbolic cross approximation*. Advanced Courses in Mathematics. CRM Barcelona. Birkhäuser/Springer, Cham, 2018. Edited and with a foreword by Sergey Tikhonov.
- [16] Hadrien De March. Entropic approximation for multi-dimensional martingale optimal transport. *arXiv preprint arXiv:1812.11104*, 2018.

- [17] Gero Friesecke, Christian B Mendl, Brendan Pass, Codina Cotar, and Claudia Klüppelberg. N-density representability and the optimal transport limit of the hohenberg-kohn functional. *The Journal of chemical physics*, 139(16):164109, 2013.
- [18] Gero Friesecke and Daniela Vögler. Breaking the curse of dimension in multi-marginal kantorovich optimal transport on finite state spaces. *SIAM Journal on Mathematical Analysis*, 50(4):3996–4019, 2018.
- [19] Alfred Galichon. A survey of some recent applications of optimal transport methods to econometrics. *The Econometrics Journal*, 20(2):C1–C11, 2017.
- [20] Alfred Galichon. *Optimal transport methods in economics*. Princeton University Press, 2018.
- [21] Didier Henrion, Jean-Bernard Lasserre, and Johan Löfberg. Gloptipoly 3: moments, optimization and semidefinite programming. *Optimization Methods & Software*, 24(4-5):761–779, 2009.
- [22] Yuehaw Khoo, Lin Lin, Michael Lindsey, and Lexing Ying. Semidefinite relaxation of multi-marginal optimal transport for strictly correlated electrons in second quantization. *arXiv preprint arXiv:1905.08322*, 2019.
- [23] Yuehaw Khoo and Lexing Ying. Convex relaxation approaches for strictly correlated density functional theory. *SIAM Journal on Scientific Computing*, 41(4):B773–B795, 2019.
- [24] Jean B Lasserre. A semidefinite programming approach to the generalized problem of moments. *Mathematical Programming*, 112(1):65–92, 2008.
- [25] Jean-Bernard Lasserre. *Moments, positive polynomials and their applications*, volume 1. World Scientific, 2010.
- [26] Charles L Lawson and Richard J Hanson. *Solving least squares problems*. SIAM, 1995.
- [27] Benedict Leimkuhler and Sebastian Reich. *Simulating hamiltonian dynamics*, volume 14. Cambridge university press, 2004.
- [28] Tony Lelièvre, Mathias Rousset, and Gabriel Stoltz. *Free energy computations: A mathematical perspective*. World Scientific, 2010.
- [29] Tony Lelièvre, Mathias Rousset, and Gabriel Stoltz. Langevin dynamics with constraints and computation of free energy differences. *Mathematics of computation*, 81(280):2071–2125, 2012.
- [30] Tony Lelièvre, Mathias Rousset, and Gabriel Stoltz. Hybrid monte carlo methods for sampling probability measures on submanifolds. *Numerische Mathematik*, 143(2):379–421, 2019.
- [31] Mathieu Lewin. Semi-classical limit of the Levy-Lieb functional in density functional theory. *C. R. Math. Acad. Sci. Paris*, 356(4):449–455, 2018.
- [32] Mathieu Lewin, Elliott H. Lieb, and Robert Seiringer. Statistical mechanics of the uniform electron gas. *J. Éc. polytech. Math.*, 5:79–116, 2018.
- [33] Mathieu Lewin, Elliott H Lieb, and Robert Seiringer. Universal functionals in density functional theory. In Éric Cancès, Gero Friesecke, and Lin Lin, editors, *Density Functional Theory*. 2019. arXiv preprint arXiv:1912.10424.
- [34] Christian B Mendl and Lin Lin. Kantorovich dual solution for strictly correlated electrons in atoms and molecules. *Physical Review B*, 87(12):125106, 2013.
- [35] Luca Nenna. *Numerical methods for multi-marginal optimal transportation*. PhD thesis, PSL Research University, 2016.

- [36] Gilles Pagès. *Numerical Probability*. Springer, 2018.
- [37] Robert G Parr. Density functional theory of atoms and molecules. In *Horizons of quantum chemistry*, pages 5–15. Springer, 1980.
- [38] Gabriel Peyré and Marco Cuturi. Computational optimal transport. *Foundations and Trends® in Machine Learning*, 11(5-6):355–607, 2019.
- [39] Federico Piazzon, Alvis Sommariva, and Marco Vianello. Caratheodory-tchakaloff subsampling. *Dolomites Research Notes on Approximation*, 10(1), 2017.
- [40] Elijah Polak. *Optimization: algorithms and consistent approximations*, volume 124. Springer Science & Business Media, 1997.
- [41] Anthony Ralston and Philip Rabinowitz. *A first course in numerical analysis*. Courier Corporation, 2001.
- [42] R Tyrrell Rockafellar. *Convex analysis*. Number 28. Princeton university press, 1970.
- [43] Giovanni Samaey, Tony Lelièvre, and Vincent Legat. A numerical closure approach for kinetic models of polymeric fluids: exploring closure relations for fene dumbbells. *Computers & fluids*, 43(1):119–133, 2011.
- [44] Filippo Santambrogio. Optimal transport for applied mathematicians. *Birkäuser, NY*, pages 99–102, 2015.
- [45] Maria Tchernychova. *Carathéodory cubature measures*. PhD thesis, University of Oxford, 2016.
- [46] Cédric Villani. *Topics in optimal transportation*. Number 58. American Mathematical Soc., 2003.
- [47] Cédric Villani. *Optimal transport: old and new*, volume 338. Springer Science & Business Media, 2008.
- [48] Daniela Vögler. Kantorovich vs. monge: A numerical classification of extremal multi-marginal mass transports on finite state spaces. *arXiv preprint arXiv:1901.04568*, 2019.
- [49] Wei Zhang. Ergodic sdes on submanifolds and related numerical sampling schemes. *ESAIM: Mathematical Modelling and Numerical Analysis*, 54(2):391–430, 2020.

A. Alfonsi UNIVERSITÉ PARIS-EST, CERMICS (ENPC), INRIA,
F-77455 Marne-la-Vallée, France
E-mail address: aurelien.alfonsi@enpc.fr

R. Coyaud UNIVERSITÉ PARIS-EST, CERMICS (ENPC), INRIA,
F-77455 Marne-la-Vallée, France
E-mail address: rafael.coyaud@enpc.fr

V. Ehrlacher UNIVERSITÉ PARIS-EST, CERMICS (ENPC), INRIA,
F-77455 Marne-la-Vallée, France
E-mail address: virginie.ehrlacher@enpc.fr